

This is a preprint.  
The final version of the work is published in  
the *Journal of Physical Oceanography*.  
<https://doi.org/10.1175/JPO-D-19-0243.1>

# Relative Dispersion in the Antarctic Circumpolar Current

Dhruv Balwada\*

*School of Oceanography, University of Washington, Seattle, Washington, USA*

Joseph H. LaCasce

*Department of Geosciences, University of Oslo, Oslo, Norway*

Kevin G. Speer

*Geophysical Fluid Dynamics Institute, Florida State University, Tallahassee, Florida, USA*

Raffaele Ferrari

*Department of Earth, Atmosphere and Planetary Sciences, Massachusetts Institute of Technology,*

*Cambridge, Massachusetts, USA*

\*Corresponding author address: Dhruv Balwada, School of Oceanography, University of Washington, Washington, WA, USA.

E-mail: [dbalwada@uw.edu](mailto:dbalwada@uw.edu)

## ABSTRACT

14     Stirring in the subsurface Southern Ocean is examined using RAFOS float  
15 trajectories, collected during the Diapycnal and Isopycnal Mixing Experiment  
16 in the Southern Ocean (DIMES), along with particle trajectories from a re-  
17 gional eddy permitting model. A central question is the extent to which the  
18 stirring is local, by eddies comparable in size to the pair separation, or non-  
19 local, by eddies at larger scales. To test this, we examine metrics based on  
20 averaging in time and in space. The model particles exhibit non-local dis-  
21 persion, as expected for a limited resolution numerical model that does not  
22 resolve flows at scales smaller than  $\sim 10$ days or  $\sim 20 - 30$ km. The different  
23 metrics are less consistent for the RAFOS floats; relative dispersion, kurto-  
24 sis and relative diffusivity suggest non-local dispersion as they are consistent  
25 with the model within error, while finite size Lyapunov exponents (FSLE)  
26 suggests local dispersion. This occurs for two reasons: (i) limited sampling of  
27 the inertial length scales and relatively small number of pairs hinder statistical  
28 robustness in time-based metrics, and (ii) some space-based metrics (FSLE,  
29  $2^{nd}$  order structure functions), which do not average over wave motions and  
30 are reflective of the kinetic energy distribution, are probably unsuitable to  
31 infer dispersion characteristics if the flow field includes energetic wave-like  
32 flows that do not disperse particles. The relative diffusivity, which is also a  
33 space-based metric, allows averaging over waves to infer the dispersion char-  
34 acteristics. Hence, given the error characteristics of the metrics and data used  
35 here, the stirring in the DIMES region is likely to be non-local at scales of  
36 5-100km.

## 37 **1. Introduction**

38 Oceanic flows are turbulent over a large range of length scales, and are very efficient at stirring  
39 tracers along isopycnals, enhancing the effects of molecular diffusion by many orders of magnitude  
40 (Garrett 2006). The parameterization of this lateral stirring is key to the proper representation of  
41 the oceanic transport of heat, carbon, nutrients and other climatically important tracers in climate  
42 models (e.g. Gnanadesikan et al. (2015); Fox-Kemper et al. (2013)). The details of these param-  
43 eterizations are particularly important in the Southern Ocean, where the surface is connected to  
44 the deep ocean via sloping isopycnals and along isopycnal stirring plays a key role in biological  
45 production (Uchida et al. 2019, 2020) and ventilation of the deep ocean (Marshall and Speer 2012;  
46 Abernathy and Ferreira 2015; Balwada et al. 2018; Jones and Abernathy 2019). To ensure the  
47 fidelity of these parameterizations it is essential that quantitative estimates of stirring are obtained  
48 using in-situ measurements.

49 The nature and strength of the lateral or along-isopycnal eddy stirring in the ocean depends on  
50 the length scales under consideration. At length scales greater than the size of dominant mesoscale  
51 eddies the stirring can approximately be expressed as enhanced molecular diffusion with a con-  
52 stant eddy diffusivity that is  $O(1000m^2/s)$  (Zhurbas and Oh 2003; Koszalka et al. 2011; LaCasce  
53 et al. 2014; Balwada et al. 2016b; Roach et al. 2016, 2018). On the other hand, at scales smaller  
54 than the typical mesoscale eddies, this eddy diffusivity generally increases with the length scale  
55 (Richardson 1926; Okubo 1971). At these scales two qualitatively different regimes are possi-  
56 ble, which can be categorized based on how stirring influences the rate of Lagrangian particle  
57 pair spreading or relative dispersion — non-local and local dispersion (Bennett 1984). Non-local  
58 dispersion occurs when the kinetic energy spectrum is steeper than  $k^{-3}$ ; in this case stirring is  
59 dominated by the largest eddies. Under local dispersion, in contrast, stirring is dominated by ed-

60 dies comparable in scale to the size of the cluster or tracer patch. Knowledge about which regime  
61 is active in the ocean can help to define parameterizations of stirring for use in eddy-permitting  
62 models (Cushman-Roisin 2008; Kämpf and Cox 2016).

63 Observational characterization of the stirring regime is practically difficult, and requires dense  
64 sampling with pairs of Lagrangian instruments, which is why most previous studies have focused  
65 on the surface ocean using surface drifters (LaCasce and Ohlmann 2003; Koszalka et al. 2009;  
66 Lumpkin and Elipot 2010; Poje et al. 2014; van Sebille et al. 2015; Sansón 2015; Beron-Vera  
67 and LaCasce 2016; Corrado et al. 2017; Essink et al. 2019). These studies have indicated that  
68 a single universal stirring regime is not present everywhere in the surface ocean; some regions  
69 show non-local dispersion up to roughly the deformation scale and others show local dispersion  
70 over the same scale range. Sometimes different metrics also lead to contrasting results in the same  
71 region. The large-scale dispersion varies as well, with some suggesting a transition to diffusive  
72 spreading — dispersion grows linearly in time — (e.g Koszalka et al. 2009) and other studies  
73 suggesting super-diffusive motion — dispersion grows faster than linear in time — most likely  
74 due to advection by the large-scale shear (e.g LaCasce and Ohlmann 2003).

75 Deep ocean studies of stirring, which are very rare, rely on sampling the flow using either an  
76 anthropogenic tracer (SF<sub>6</sub>) (Ledwell et al. 1998; Watson et al. 2013) or RAFOS floats (Rossby  
77 et al. 1986). While a tracer is an excellent means for measuring diapycnal diffusivities (Ledwell  
78 et al. 2000; Watson et al. 2013; Ledwell et al. 2016), sampling the details of the lateral spatio-  
79 temporal evolution of the tracer by ships is not usually possible and thus limits its usefulness for  
80 diagnosing the scale dependence of lateral stirring. RAFOS floats (Swift and Riser 1994), which  
81 drift at depth and are acoustically tracked, can be used to characterize and quantify the properties  
82 of stirring by evaluating how rapidly float pairs disperse. We are aware of only two previous  
83 studies that reported on relative dispersion in the deep ocean (LaCasce and Bower 2000; Ollitrault

84 et al. 2005), both in the North Atlantic Ocean at depths of about 1 km. LaCasce and Bower  
85 (2000) concluded the dispersion in the western Atlantic was either local or driven by mean flow  
86 shear up to scales of approximately 100km, while the particle pairs separated diffusively in the  
87 eastern Atlantic. Ollitrault et al. (2005) also reported local stirring between 40-300km, and some  
88 indications of non-local stirring at shorter scales.

89 In this study, we examine stirring at length scales of 5 – 100 km and depths of 500 – 2000 m  
90 in the Southeast Pacific Ocean sector of the Antarctic Circumpolar Current (ACC), using RAFOS  
91 floats deployed during the Diapycnal and Isopycnal Mixing Experiment in the Southern Ocean  
92 (DIMES) (Balwada et al. 2016b). The floats were deployed in pairs and triplets to resolve smaller  
93 scale dispersion. This work builds on the studies by Tulloch et al. (2014); LaCasce et al. (2014);  
94 Balwada et al. (2016b), which had reported on the eddy diffusivity in the DIMES experiment using  
95 both tracer and float observations at scales larger than the dominant mesoscale eddies.

96 To quantify the flow variability and stirring in the DIMES region we use several different met-  
97 rics. We start by quantifying the flow variability at different scales using Lagrangian frequency  
98 spectra and  $2^{nd}$  order structure functions in section 3. Stirring or particle dispersion is a result  
99 of the integrated effect of the flow variability, and is usually quantified and categorized as local  
100 vs non-local using metrics that either quantify temporal evolution or spatial structure (Table 1).  
101 The pair separation probability distribution function (PDF), and its moments, e.g. the relative dis-  
102 persion and kurtosis, fall under the time-based metrics. These quantify the temporal evolution of  
103 the separation between pairs of particles and are discussed in section 4. The relative diffusivity,  
104 discussed in section 5, quantifies the rate of change of relative dispersion. As the averages are  
105 conditioned by separation, the relative diffusivity is a space-based metric. Finite size Lyapunov  
106 exponent (FSLE), discussed in section 6, quantifies the rate at which particle pairs at different  
107 scales separate and is also a space-based metric. Space-based metrics advantageously employ

108 more and more pairs at larger separations; since the same pairs usually visit the larger scales more  
109 often than the smaller scales. In contrast, the time-based metrics are limited at all time by the  
110 number of samples at the initial pair separation. A summary of the different metrics is presented  
111 in Table 1, and Table 2 provides a quick overview of the results.

## 112 **2. Data and Methods**

### 113 *a. Lagrangian Trajectories*

114 We examine two sets of Lagrangian trajectories: RAFOS floats released during the DIMES  
115 experiment (Balwada et al. (2016b)), and numerical particles advected in a MITgcm simulation of  
116 the Southeast Pacific Ocean and Scotia Sea (LaCasce et al. (2014)).

117 The DIMES RAFOS floats, referred to as the floats in the rest of the manuscript, were released  
118 along the  $105^{\circ}\text{W}$  meridian and between  $54^{\circ} - 60^{\circ}\text{S}$ , spanning the ACC at this location (Figure 1a).  
119 Acoustic tracking was used to determine their position once per day. The motion of the floats was  
120 primarily along isobars, and they were spread over a depth range of 500 - 2000 m, with the greatest  
121 sampling near depths of 750m and 1400m (Figure 1c). In this study we grouped the floats into two  
122 depth bins: shallow (500-1000 m) and deep (1000-1800 m), and only considered segments of the  
123 trajectories to the west of  $80^{\circ}\text{W}$ . The data to the east of  $80^{\circ}\text{W}$ , in the Scotia Sea, are not considered  
124 because the floats there rarely came within 100km of each other.

125 The MITgcm numerical particles, referred to as particles in the rest of the manuscript, are the  
126 same as those used in LaCasce et al. (2014) (Figure 1b). The velocity fields used to advect the par-  
127 ticles were simulated using the MITgcm with a horizontal resolution of 5km and 70 vertical levels.  
128 The model domain spanned  $160^{\circ} - 20^{\circ}\text{W}$  and  $75^{\circ} - 35^{\circ}\text{S}$ , and was forced at the lateral bound-  
129 aries by the Ocean Comprehensive Atlas (OCCA, Forget (2010)) and at the surface by ECMWF

130 ERA-Interim 6h wind fields (Berrisford et al. 2009). Details of the simulation and comparison to  
131 hydrography can be found in Tulloch et al. (2014). 100 particles were released along  $105^{\circ}W$  at 20  
132 vertical levels, between  $55^{\circ} - 60^{\circ}S$ , at the numerical grid separation of 5km every 10 days for 120  
133 days - 12 releases totaling to 1200 particles. The particles were advected using one-day averaged  
134 3D velocity fields, since the model had negligible variance at faster time scales. Correspondingly,  
135 the particle positions were saved at a daily resolution. This provided 1200 particle trajectories at  
136 each of the 20 levels from 300 m to 3000 m.

137 The velocity time series following the float and particle trajectories was calculated using discrete  
138 forward differences ( $u(t) = \frac{x(t+\delta t) - x(t)}{\delta t}$ ), except at the end points where a backward difference was  
139 used. As the temporal resolution of the floats ( $\delta t$ ) is 1 day, the variability at periods faster than 1  
140 day (the inertial period is 14 hours in this region) is aliased to longer periods.

#### 141 *b. Pair Selection*

142 In this study, two different kinds of metrics are considered; time-based metrics average at fixed  
143 time and space-based metrics average at fixed spatial scales. The time-based metrics, such as  
144 relative dispersion, are a conditional average over pairs with the same initial pair separation ( $r_0 \pm$   
145  $\delta$ ), and this averaging is indicated by  $\langle \cdot \rangle_{r_0}$ . The space-based metrics, such as structure functions,  
146 relative diffusivity and finite size Lyapunov exponents, average over all pairs that pass through a  
147 separation bin, irrespective of the initial pair separation, and this averaging is indicated by  $\langle \cdot \rangle$ .

148 Selecting pairs for time-based metrics conditioned on initial separation ( $\langle \cdot \rangle_{r_0}$ ) is trivial in the  
149 numerical model because the particles were initialized on a discrete grid. We use particle pairs that  
150 were initially released at the same depth and at a particular  $r_0$ . When considering the observations,  
151 a few choices need to be made due to the following considerations: the floats are not released on

152 a uniform grid, the floats are not all at the same depth due to slight irregularities in instrument  
153 ballasting, and there are some gaps in the float time series due to tracking problems.

154 When analyzing the floats, we use pairs that might be an original pair, a pair released together,  
155 or a chance pair, a pair that happens to pass in close proximity ( $r_0 \pm \delta r$ ) due to the flow, and we  
156 do not distinguish between the two in the rest of this study (Morel and Larceveque 1974; LaCasce  
157 and Bower 2000). We chose  $r_0$  to be relatively large to ensure that sufficient number of pairs are  
158 available; this caused most pairs to be chance pairs as most original pairs were released at smaller  
159 initial separation. In some cases a pair time series might return to a separation of  $r_0$  at a later  
160 time; we considered this to be the origin of a new chance pair time series if this return happened at  
161 least 25 days after the first time the pair members were  $r_0$  apart. However, instances of this were  
162 rare and did not contribute significantly to the samples used in this study. We use pair time series  
163 with a length of 100 days, since the pair velocities generally decorrelate before that time (shown  
164 later). Any pair with less than 25 days of data during this 100 day period is discarded. Finally, to  
165 minimize the impact of vertical shear on the separation rates we divided the floats into a shallow set  
166 (500-1000 m) and a deep set (1000-1800 m), and only considered pairs with trajectories vertically  
167 within 200 m of each other.

168 Two initial float separation sets, 10-15 km and 30-35 km, were chosen to allow for sufficient  
169 sampling. The first baroclinic deformation radius in this region is approximately 15 km (Chelton  
170 et al. 1998), hence the smaller initial separation set partially sampled this scale (Figure 1c-e). The  
171 shallow sets (500-1000 m) contain approximately 50 and 100 pairs in the two  $r_0$  bins, and the deep  
172 sets (1000-1800 m) contain approximately 90 and 180 pairs in the two  $r_0$  bins. The number of  
173 pairs in each set did not vary substantially over the course of the 100 days considered here. Most  
174 pairs evolved at vertical separations of less than 50 m. Since most of the strong vertical shear in the  
175 interior ocean is associated with high-frequency wave-like motions that do not cause much lateral



176 dispersion, we anticipate the impact of this high frequency vertical shear on most of the dispersion  
177 metrics to be small. Further, the mean vertical shear in this region is approximately  $O(10^{-4}s^{-1})$   
178 (Balwada et al. 2016a), which can result in a net dispersion on the order of  $10km^2$  in 10 days and  
179  $10^3km^2$  in 100days, which is negligible compared to the observed relative dispersion (Figure 5).

180 The corresponding particle analysis was performed on particle pairs that were released at initial  
181 separations of 11.1km and 33.3km. There are 20 sets of model particles released between 500-  
182 2000m and each set was composed of between 1100-1200 pairs. In most of the sections we  
183 focused on particles released at depths of 750m and 1500m. These set of particles are qualitatively  
184 similar — have similar time scales and scaling relationships — to the shallow and deep sets of  
185 floats, but an exact quantitative match should not be expected. In section 3, where we quantify the  
186 variability, we selected depths that enclose the two sampled ranges, 500 and 900m corresponding  
187 to the shallow set and 1100 and 1700m corresponding to the deep set.

188 For all space-based metrics, which parse data along a separation axis ( $\langle \cdot \rangle$ ), we defined separation  
189 bin edges as  $r(n) = a^n r(0)$ , where  $a = 1.4$  and  $r(0) = 1$  km. For floats, we only used pairs that  
190 were separated by less than 100m in the vertical. The number of float pairs in each bin for the  
191 shallow and deep set are shown in Figure 1f. The number of pairs increase from less than 100 at  
192 the smallest separation to close to 10,000 at separations of 300km, with the deeper set having more  
193 pairs. For the particles more than 1000 pairs were available for each separation bin (not shown).

194 All *error bars* in this study are derived using the bootstrapping algorithm. We estimate the  
195 metric 1000 times, performing random draws with repetition, and use the 5<sup>th</sup> and 95<sup>th</sup> percentiles  
196 as the limits of the error bars.

### 197 **3. Temporal and Spatial Flow Variability**

198 In this section, we quantify the distribution of the kinetic energy at different temporal and spatial  
199 scales. This will provide a helpful context to the stirring metrics that will be discussed later.

#### 200 *a. Rotary Lagrangian Frequency Spectra*

201 Rotary spectra decompose the power in the velocity time series into counterclockwise (posi-  
202 tive frequencies) and clockwise (negative frequencies) motions at different time scales (Thomson  
203 and Emery 2014), which correspond to anticyclonic and cyclonic motions in the Southern Hemi-  
204 sphere respectively. Here we perform this spectral decomposition on the velocity following the  
205 Lagrangian trajectory, using trajectory segments of 120 days and the multitaper method (Lilly  
206 2019).

207 The float rotary spectra show a plateau at low frequencies, transitioning to a power law behavior  
208 with slope of about -4 at intermediate frequencies (Figure 2 a,b). At frequencies higher than 1/10  
209 days<sup>-1</sup> a much flatter power law is observed. This flattening of the spectra at high frequencies  
210 can potentially be attributed to internal waves, near inertial waves (NIWs), tides, which have  
211 been aliased to these frequencies, and some contributions from the position tracking errors. The  
212 cyclonic and anticyclonic components of the float spectra are almost indistinguishable, with no  
213 preference for a particular polarization, and the spectral energy at the shallower depths is higher  
214 than at greater depths.

215 At the lower frequencies, the behavior of the particle spectra is similar to the float spectra, with  
216 the low frequency plateau from the observations lying within the range of energy levels from the  
217 model at comparable depths (Figure 2a,b). A power law regime, with a slope of approximately -5,  
218 extends from intermediate to high frequencies. Thus, the model spectra lacks the high frequency

219 flattening seen in the observations, which is a result of limited model resolution and the daily  
 220 averaged velocities used to advect the particles.

221 *b. Longitudinal Velocity Structure Function*

222 Second order velocity structure functions represent flow correlations across spatial scales, and  
 223 are related to the kinetic energy spectra (Babiano et al. 1985; LaCasce 2016). The longitudinal  
 224 second order structure function is defined as:

$$S2_{ll}(r) = \langle (\delta \mathbf{u}(r) \cdot \hat{\mathbf{r}})^2 \rangle, \quad (1)$$

225 where  $\delta \mathbf{u}(r) = \mathbf{u}(\mathbf{x} + r) - \mathbf{u}(\mathbf{x})$  is the velocity difference between two particles separated by dis-  
 226 tance  $r$ ,  $\hat{\mathbf{r}}$  is the unit vector connecting these two particles. We assume homogeneity and isotropy  
 227 to drop the dependence on  $\mathbf{x}$  and  $\hat{\mathbf{r}}$  respectively.

228 The second order longitudinal structure function is related to the longitudinal frequency-  
 229 wavenumber spectrum ( $E_{ll}(k, \omega)$ ) via,

$$S2_{ll}(r) = 2 \int_0^\infty \left[ \int_0^\infty E_{ll}(k, \omega) d\omega \right] (1 - J_0(kr)) dk, \quad (2)$$

230 where  $k$  is the horizontal wavenumber,  $J_0()$  is the zeroth order Bessel function. Thus  $S2_{ll}(r)$   
 231 has contributions, filtered by the Bessel function, from all wavenumbers and frequencies. If the  
 232 wavenumber energy spectrum follows a power law ( $E_{ll}(k) = \int_0^\infty E_{ll}(k, \omega) d\omega \sim k^{-\alpha}$ ) over a long  
 233 enough range of scales and  $1 < \alpha < 3$ , then the integral is dominated by wavenumbers near  $k \sim 1/r$   
 234 and the structure function follows a power law ( $S2_{ll}(r) \sim r^{\alpha-1}$ ). While, if  $\alpha > 3$  then  $S2_{ll}(r) \sim r^2$   
 235 for all  $n$  (Bennett 1984; Balwada et al. 2016a). At scales where the velocities are uncorrelated the  
 236 structure function is constant and equals twice the velocity variance.

237 Both shallow and deep float  $S2_{ll}$  (Figure 2c,d) approach a constant at scales larger than approx-  
 238 imately 200 km, with this length scale being slightly larger for the shallower floats. The kinetic

239 energy level, the large scale constant value of  $S2_{II}$ , observed by the shallower floats is approxi-  
240 mately 3 times greater than the deeper floats. For the shallow floats,  $S2_{II}$  follows a power law of  
241 approximately  $r^1$  between separation of 20-100km, and becomes flatter at smaller scales. For the  
242 deep floats  $S2_{II}$  follows a power law that is slightly flatter than the shallower floats, and closer to  
243  $r^{2/3}$ .

244 In contrast, the model structure functions are similar to those expected for a flow with a kinetic  
245 energy spectrum steeper than  $k^{-3}$ , with a power law behavior of  $r^2$  at small scales and transitioning  
246 to uncorrelated motions at scales larger than about 100-200km. The kinetic energy level decreases  
247 with depth similar to observations.

248 Thus the structure functions also indicate energy at small scales present in the observations but  
249 not in the model. This is true for scales less than roughly 20 km and for times less than about a  
250 week.

## 251 **4. Relative Dispersion and Kurtosis**

### 252 *a. Theory*

253 The characteristics of the stirring are encoded in how the separation between particle pairs  
254 evolves, and can be quantified by considering the evolution of pair separation PDF and its mo-  
255 ments: relative dispersion (2nd moment), which is a measure of the size of the tracer cloud, and  
256 kurtosis (normalized 4th moment).

257 The relative dispersion, the mean square pair separation, evolution can be derived using purely  
258 kinematic arguments (Babiano et al. 1990). These are based on the relative diffusivity, the the

259 derivative of the relative dispersion  $\overline{r^2}$ ,

$$\begin{aligned} \kappa(t|r_0) &\equiv \frac{1}{2} \frac{d\overline{r^2}(t|r_0)}{dt} \\ &= \langle \mathbf{r}_0 \cdot \delta \mathbf{V}(t|r_0) \rangle_{r_0} + \int_0^t \langle \delta \mathbf{V}(t|r_0) \cdot \delta \mathbf{V}(\tau|r_0) \rangle_{r_0} d\tau, \end{aligned} \quad (3)$$

260 where  $\delta \mathbf{V}(t|r_0)$  is the relative velocity of a pair, and the dependence on the initial condition  $r_0$  is  
 261 explicitly noted. For flow randomly seeded with particles, the correlation of the first term of the  
 262 RHS is typically small, as it was for both particles and floats (not shown). At short times ( $t \rightarrow 0$ ),  
 263 equation 3 is approximated as  $\kappa(t|r_0) \approx t S_{2II}(r_0)$ , and the relative dispersion grows ballistically  
 264 ( $\overline{r^2} = r_0^2(1 + C_1 t^2)$ , where  $C_1$  is a constant proportional to the total enstrophy). At large times  
 265 ( $t \rightarrow \infty$ ), the relative velocities are uncorrelated ( $\langle |\delta \mathbf{V}(\infty)|^2 \rangle_{r_0} = 4KE$ ). If the integral of the time  
 266 correlation of the relative velocities converges, then the relative dispersion grows linearly ( $\overline{r^2} \sim t$ )  
 267 as for a diffusive process (Taylor 1922).

268 Of primary interest are the scales at intermediate times, when pair separations lie in the inertial  
 269 range and pair velocities are still correlated. Here, the stirring properties can be well quantified  
 270 using the pair separation PDF, from which the relative dispersion derives. The separation PDF can  
 271 be modeled using a Fokker-Plank (FP) equation (Richardson 1926; Bennett 2006),

$$\frac{\partial}{\partial t} p = \frac{1}{r} \frac{\partial}{\partial r} \left( r \kappa \frac{\partial}{\partial r} p \right), \quad (4)$$

272 where  $p(r, t)$  is the pair separation PDF, and  $\kappa(r)$  is a diffusivity as a function of separation  $r$ .  
 273 The  $n^{th}$  raw moment of the PDF is defined as  $\overline{r^n}(t) = 2\pi \int_0^\infty r^{n+1} p(r, t) dr$ . This equation can be  
 274 solved for the turbulent inertial ranges (LaCasce 2010; Graff et al. 2015), assuming all particle  
 275 pairs have the same separation initially. The inertial range slope enters via the relative diffusivity  
 276 ( $\kappa(r)$ ), which can be inferred from scaling. For shallow-sloped KE spectra, where  $1 < \alpha < 3$ , the  
 277 diffusivity scales  $\kappa(r) \propto r^{(\alpha+1)/2}$ , and the dispersion is characterized as "local". For steeply sloped  
 278 KE spectra,  $\alpha \geq 3$ , the relative diffusivity scales as  $\kappa(r) \propto r^2$ , and the dispersion is "non-local".

279 When solving the FP equation, it is assumed the same diffusivity applies across all scales. We  
 280 list the analytical expressions for the PDF, the relative dispersion and kurtosis for the non-local  
 281 regime, the Richardson regime (a particular local regime), and the diffusive regime in Table 1.

### 282 *b. Correlation and Isotropy from Floats and Particles*

283 Correlated pair velocities are expected at scales smaller than those of the largest eddies. We  
 284 define a pair velocity correlation coefficient,  $\rho(t|r_0) = \frac{\langle \mathbf{u}_1(t) \cdot \mathbf{u}_2(t) \rangle_{r_0}}{\langle |\mathbf{u}_1(t)| \rangle_{r_0} \langle |\mathbf{u}_2(t)| \rangle_{r_0}}$ , which can vary between  
 285 -1 and 1. The subscripts on the velocity correspond to two members of the pair. As expected,  
 286  $\rho(t|r_0)$  for floats and particles generally decreases as a function of time, and the maximum value  
 287 of  $\rho$  decreases as a function of initial separation (Figure 3a,b). Moreover, the rate of decrease is  
 288 more rapid for the shallower sets than the deeper sets.

289 Alternatively the correlation can be visualized as a function of spatial scale by plotting  $\rho(t|r_0)$   
 290 against the corresponding mean pair separation ( $r^* = \sqrt{r^2(t|r_0)}$ ) (Koszalka et al. 2011; Graff et al.  
 291 2015). This causes all the  $\rho(r^*)$  curves to approximately collapse together (Figure 3c), suggesting  
 292 that the decrease in correlation over time is a result of pairs exiting the range of length scales  
 293 over which the flow is correlated. This explains why the correlation drops more rapidly for the  
 294 shallower depths, as the particles disperse faster there. The collapsed curves fall below 0.5 at a  
 295 length scale ( $r^*$ ) of approximately 60-70km.

296 Most relative dispersion theory assumes the flow is isotropic. We quantify isotropy as a ratio  
 297 of the square root of the mean zonal separation to the square root of the meridional separation  
 298 ( $|r_x^*|/|r_y^*|$ ) (Morel and Larceveque 1974); this is one if the zonal and meridional spreading is the  
 299 same. For the shallow floats and particles the ratio exceeds 1 after about 50 days (Figure 4a) and  
 300 at length scales greater than 100 km (Figure 4c), while for the deeper sets the ratio stays close to  
 301 1 over 100 days (Figure 4b). The only exception is the shallow float set with  $r_0 \sim 10 - 15$ km that

302 shows enhanced zonal dispersion after only 10 days (though there are fewer than 50 pairs in this  
303 group). The particles always exhibit a small ratio for the first few days, which is due to the particles  
304 being deployed along a longitude line. Thus the dispersion is nearly isotropic at scales where the  
305 velocities are correlated. Isotropy is discussed further in the section on relative diffusivity (section  
306 5b), where we show more conclusively that the flow is isotropic at length scales smaller than  
307 approximately 100km.

### 308 *c. Relative Dispersion and Kurtosis from Floats and Particles*

309 Due to the small number of float pairs, it is difficult to draw conclusions about PDFs themselves.  
310 The float PDFs are statistically indistinguishable from both the non-local and Richardson (local)  
311 theoretical PDFs (Table 1), while the particle PDFs are suggestive of non-local dispersion. Details  
312 are given in appendix B.

313 The relative dispersion increases in time, showing that on average the floats and particles dis-  
314 perse (Figure 5a,d). The dispersion for the floats and particles is very similar over the first 100  
315 days, suggesting the additional high-frequency and small-scale variability in the ocean does not  
316 contribute much dispersion. At the shallower depth the relative dispersion increased to  $300^2\text{km}^2$   
317 by the end of the 100 days for both initial separations, while the deeper relative dispersion is less.  
318 Towards the end of the 100 days the dispersion for most sets has transitioned to a diffusive linear  
319 growth.

320 Under Richardson dispersion, the squared separations would grow cubically in time. However,  
321 this asymptotic limit can not be achieved in the ocean because of the finite size of the inertial  
322 ranges. The exact expression for the Richardson dispersion at all times was derived in Graff et al.  
323 (2015) (presented in Table 1), and is relatively complex. However, we found (not shown) that the  
324 less rigorous but simpler expression,  $(r_0^{2/3} + C_2t)^3$ , derived by Ollitrault et al. (2005) is visually

325 indistinguishable from the more complex expression, when both are plotted in a compensated  
326 form:  $(\overline{r^2}^{1/3} - r_0^{2/3})$ . This form, based on the expression from Ollitrault et al. (2005) removes  
327 the dependence on initial condition and has a slope of one on a log-log plot under Richardson  
328 dispersion. This compensated relative dispersion from the floats and particles does not show a  
329 distinct linear range (figure 5c, f). Generally, the growth rate is faster than the expectation from  
330 Richardson dispersion initially and then slower. A short range from approximately 6-20 days for  
331 the shallower sets and 15-30 days for the deeper sets shows a growth rate that might be comparable  
332 to Richardson dispersion, but it is more likely that this is simply a transition period. The shallow  
333 float set with  $r_0 \sim 10 - 15\text{km}$  is a slight exception, since it approximately matches with Richardson  
334 dispersion from 2-40 days (also true for kurtosis discussed next). As noted though this set has few  
335 pairs, and thus the approximate match to Richardson dispersion may not be robust.

336 If the dispersion were non-local, it would grow exponentially in time. The relative dispersion,  
337 for both floats and particles, increases rapidly for the first 10-25 days and then settles into a slower  
338 growth afterwards (figure 5 b,e). The initial growth is not distinguishable from exponential. For  
339 example, the relative dispersion for the shallow particles with  $r_0 = 11\text{km}$  between 4-15 days sug-  
340 gests that exponential growth occurs up to approximately length scales of  $\sim 5r_0 \approx 55\text{km}$ . Similar  
341 phases of exponential growth are also seen at other depths for the particles, and to some degree  
342 for the floats. This rapid growth ends when the mean separation reaches  $r^* \sim 50 - 90\text{km}$  for all  
343 cases considered, and is thus shorter for larger  $r_0$ . The relative dispersion from the particles for the  
344 first 3-4 days shows a slightly slower growth rate, which is likely a result of dependence on initial  
345 conditions and a short phase of ballistic growth (see further discussion in Appendix B).

346 Under non-local dispersion, the kurtosis also grows exponentially, while it asymptotes to 5.6  
347 under 2D Richardson dispersion; it asymptotes to 2 if the dispersion is diffusive (Table 1) (LaCasce



2010). Local dispersion with a spectral slope between -3 and -5/3 can also result in kurtosis surpassing 5.6 (Foussard et al. 2017).

The kurtosis from the floats and particles evolves similarly, with a rapid initial increase for approximately 10-20 days followed by a decay towards 2 (Figure 6). The kurtoses do not rise to very large values because  $r_0$  is large. The pairs in the tails of the PDFs transition to the uncorrelated regime at about 10-20 days (Figure B1), so that the kurtosis could not rise to large values even under exponential initial growth. Thus one cannot distinguish local or non-local dispersion at small scales based on the kurtosis. But the similarity between float and particle kurtoses suggest the floats disperse similarly to the particles.

Thus the displacement moments from the floats and particles are similar within the errors. However, it is difficult to distinguish the exact type of dispersion occurring at small scales. This is likely due to the relatively large initial separations,  $r_0$ . Next we consider space-based metrics, which average without any conditioning on  $r_0$ .

## 5. Relative Diffusivity

Now we examine the relative diffusivity. The initial separation,  $r_0$ , is used to assign the spatial scale, so that  $\kappa(r) \approx \kappa(t|r_0)$  (equation 3). We estimate  $\kappa(r)$  using finite difference,

$$\kappa(r) = \kappa(\Delta t/2|r_0) \approx \frac{d\overline{r^2}(\Delta t/2|r_0)}{dt} \approx \frac{\overline{r^2}(\Delta t|r_0) - \overline{r^2}(0|r_0)}{\Delta t}. \quad (5)$$

It is possible to use different time spacings,  $\Delta t$ . We will vary this to estimate the longer time estimate of relative diffusivity and to filter high frequency motions in the observations. It should also be small enough so that the diffusivity is less than the asymptotic value of twice the single particle diffusivity (LaCasce 2008). The single particle integral time scale for the region is approximately 5-6 days (Balwada et al. 2016b); as discussed below, this works well as a practical

369 estimate of  $\Delta t$ . Further consideration about the link between second order structure function and  
370 relative diffusivity, effects of the high frequency motions, and theoretical guidance for varying  $\Delta t$   
371 is given in Appendix C.

372 We first examine the dependence of  $\kappa(r)$  on  $\Delta t$  using the model particles. The diffusivities  
373 for the shallow and deep particles with  $\Delta t = 1\text{day}$  increase as  $r^2$ , up to scales of approximately  
374 50-60km, in line with a steep spectrum. At larger scales the diffusivity flattens out. At still larger  
375 scales, the diffusivity increases again, approximately as  $r^{4/3}$  (Figure 7a). This power law depen-  
376 dence for the particles between 6-50km is not very sensitive to  $\Delta t$  up to moderate values,  $\sim 6\text{days}$   
377 for shallow and  $\sim 10\text{days}$  for deep particles, but flattens out with larger  $\Delta t$ . This follows as pairs  
378 with smaller  $r_0$  start to experience more uncorrelated motion and the relative diffusivity asymp-  
379 totes to the large scale diffusivity (Figure 7c). Increasing  $\Delta t$  to 6days increases the magnitude  
380 of the diffusivity for separations between 6-50km, because at 6days the pairs are sampling larger  
381 scales than  $r_0$  with larger diffusivities, but this does not change the power law dependence signif-  
382 icantly. The choice to plot the results hereafter using 6 days is a pragmatic one; the slope of the  
383 relative diffusivity of the shallow particles is not very sensitive within this time frame, and 6 days  
384 is similar to the single particle integral time scale for the floats in this region.

385 The float-derived diffusivities exhibit a different dependence on  $\Delta t$  (Figure 7a,b,c). With  $\Delta t =$   
386 1day,  $\kappa(r)$  exhibits a power law dependence close to  $r^{4/3}$  at scales smaller than 100km. This is  
387 consistent with  $S2_{II}(r)$  being flatter ( $\kappa(r,t) \approx tS2_{II}(r)$  at short times, Babiano et al. (1990)). As  $\Delta t$   
388 is increased, the curve steepens (Figure 7c), and over a range of intermediate values of  $\Delta t$  agrees  
389 well with the power law of the particle diffusivity down to scales of 5km. This suggests increasing  
390  $\Delta t$  acts as a filter, removing the high frequency motions that cause the relative diffusivity power  
391 law from the floats to be flatter than that of the particles at short times. As with the particles, when  
392  $\Delta t$  is increased further ( $\Delta t > 15\text{ days}$ ) the slope flattens, as the influence of the uncorrelated scales

393 becomes more dominant. It should be noted that a perfect match between the relative diffusivity  
394 slope dependence on  $\Delta t$  from floats and particles at these longer  $\Delta t$  should not be expected,  
395 because the floats are spread over a depth range and the particle depths were chosen to only match  
396 the float depth approximately (section 2).

397 Thus the high frequency motions present in the observations are responsible for the diffusivity's  
398 weaker dependence on  $r$  (local dispersion) when the evolution of the pairs over a short time period  
399 is considered. However, the diffusivity's dependence on  $r$  steepens (non-local dispersion) when the  
400 evolution of the same pairs over a few days is considered; indicating that the smaller scales have  
401 a relatively weaker net impact as some of the higher frequency pulsation in separation averages  
402 out to zero. We find that wave-like motions are a likely process that can result in this observed  
403 behavior for the relative diffusivity, as detailed in Appendices A and C.

404 As the mean flow here is nearly zonal (LaCasce et al. 2014; Balwada et al. 2016a), the zonal  
405 and meridional diffusivities reflect the stirring along and across the mean flow. Using the longer  
406 differencing time ( $\Delta t = 6$  days), the zonal and meridional diffusivities for the floats and particles  
407 are very similar, suggesting isotropy up to roughly 100 km separations (Figure 8a,c). At larger  
408 scales, the zonal and meridional diffusivities diverge as the flow becomes anisotropic and pair  
409 velocities are uncorrelated. The zonal diffusivity continues growing with a scaling close to  $r^{4/3}$ .  
410 This anisotropic growth could be indicative of shear dispersion (Bennett 1984; LaCasce 2008). At  
411 these scales of uncorrelated motion the meridional diffusivity approaches a constant value close  
412 to twice the single particle diffusivity estimate for the region (LaCasce et al. 2014; Balwada et al.  
413 2016b). At the correlated scales, the meridional relative diffusivity is an increasing function of  
414 separation scale and time scale ( $\Delta t$ ) and is greater at the shallower depth (Figure 8 b,d).

415 Some studies (e.g. Sinha et al. (2019); Sansón (2015) most recently), estimate the scale depen-  
416 dence of relative diffusivity by differentiating the relative dispersion time series for a particular

417 initial separation and assigning the mean separation ( $r^*(t)$ ) as the spatial scale ( $\kappa(r^*|r_0)$ ). Using  
 418 this estimate (Figure 7d), we were even unable to detect  $r^2$  regime for the particles, possibly since  
 419 the average occurs over a wider range of scales. This estimate was very noisy for the floats.

## 420 6. Finite Size Lyapunov Exponents

### 421 a. Theory

422 Finite Size Lyapunov Exponents (FSLE) is an alternate way of quantifying stirring, and mea-  
 423 sures the average time taken ( $\langle \tau(r) \rangle$ ) for a pair of particles to grow in separation from scale of  $r$  to  
 424  $ar$ , where  $a > 1$  (Artale et al. 1997). FSLE ( $\lambda$ ) is defined as

$$\lambda(r) = \frac{\log(a)}{\langle \tau(r) \rangle}. \quad (6)$$

425 Theoretical scalings for FSLE can be derived based on dimensional arguments. If the stirring is  
 426 local and the energy spectrum follows a power law of  $k^{-\alpha}$  ( $\alpha < 3$ ), then the FSLE scales as  
 427  $\lambda(r) \propto r^{(\alpha-3)/2}$ . Thus for Richardson dispersion the FSLE scales as  $\lambda(r) \propto r^{-2/3}$ . For  $\alpha \geq 3$ , the  
 428 FSLE converges to a constant ( $\lambda(r) \propto r^0$ ), and for uncorrelated diffusive spreading  $\lambda(r) \propto r^{-2}$ .  
 429 These are summarized in Table 1.

### 430 b. FSLE from Floats and Particles

431 The floats were tracked daily, and the output of the particles was saved daily. This sets an  
 432 artificial discretization on the possible values of  $\lambda$ , which would particularly be an issue at smaller  
 433  $r$  when particle pairs will separate to  $ar$  in one or two time steps. To alleviate this issue, we linearly  
 434 interpolated the separation time series between the resolved times (LaCasce 2008; Lumpkin and  
 435 Elipot 2010; Haza et al. 2014). The interpolation caused an increase in the value of the FSLE for  
 436 floats, and also slightly steepened the power law behavior at smaller scales (not shown). The linear

437 interpolation also increases the value of FSLE slightly for the particles, but does not change the  
438 power law behavior of FSLE (not shown). The FSLE estimated using the linear interpolation was  
439 not sensitive to the size of the bins (value of  $a$ , which is chosen to be 1.4 here).

440 The FSLE from the floats shows an approximate  $-2/3$  dependence at scales smaller than 100km,  
441 at both the shallow and deep levels (Figure 9). At scales larger than 100km the FSLE slope  
442 becomes steeper, tending towards  $-2$ . The FSLE from the particles at scales smaller than 100km  
443 is almost flat, and markedly different from the floats. At scales greater than 100km the FSLE  
444 from particles is almost identical to that from floats. At the shortest scales, smaller than the model  
445 resolution, the particle FSLE slightly diverges from a constant, which is presumably a result of  
446 interpolation used in particle tracking. There is no qualitative difference between the results of the  
447 shallow and deep sets, except for the time scales being faster at shallower depth.

448 The results suggest the floats experience local dispersion and the particles non-local dispersion  
449 at scales smaller than 100km. Both exhibit diffusive spreading at larger scales. The time scale  
450 associated with the FSLE at small scales is 1 to 10 days, which is where the high frequency  
451 motions appear in the observations (section 2). So these motions are likely associated with the  
452 local dispersion seen here.

453 We consider the effects of high frequency motion on the FSLE further in Appendix A. We show  
454 that wave energy at time scales shorter than a day can be aliased to scales of 1-10 days when the  
455 temporal resolution is a day; and this aliased energy can potentially cause the FSLE to appear  
456 local even when the dispersion is a result of non-local stirring. Thus, we cannot conclude based  
457 on the float FSLE that the dispersion is local, but the characterization of the particle FSLE being  
458 non-local is appropriate.

## 459 **7. Discussion**

460 The Southeast Pacific Ocean sector of the ACC, between the mid-ocean ridge and Drake Pas-  
461 sage, was sampled by a subset of DIMES RAFOS floats and simulated with an eddy-permitting  
462 model. We provide an observational perspective on turbulent stirring in the ACC at length scales  
463 comparable to and smaller than the mesoscale eddies, in one of the few observational studies that  
464 addresses relative dispersion in the deep ocean. The stirring is quantified using time-based and  
465 space-based metrics (summarized in Table 2).

466 At scales comparable to and larger than the mesoscale eddies the pair velocities are uncorrelated  
467 and the dispersion is anisotropic. The meridional dispersion behaves like random walk and zonal  
468 dispersion behaves like shear dispersion. The meridional relative diffusivity saturates at a value  
469 near  $1000m^2/s$ , in agreement with single particle-based estimates (Balwada et al. 2016b; LaCasce  
470 et al. 2014; Tulloch et al. 2014). This is approximately two orders of magnitude larger than the  
471 relative diffusivity at scales smaller than 10km, in agreement with the estimates based on DIMES  
472 tracer roughness (Boland et al. 2015).

473 At scales smaller than the mesoscale eddies the pair velocities are correlated and the dispersion  
474 is isotropic. Under these conditions the stirring can be characterized as local, primarily influenced  
475 by eddies at the scales of the pair separations, or non-local, primarily influenced by eddies that are  
476 much bigger than the scales of the pair separations. Overall, we concluded that the RAFOS floats  
477 likely experienced non-local stirring at scales longer than a few inertial periods and approximately  
478 5km in this part of the ocean, since at these scales their dispersion is broadly similar to that of non-  
479 locally dispersed model particles. However, some important distinctions between the different  
480 time- and space-based metrics for the floats and particles are present.

481 The time-based metrics, relative dispersion and kurtosis, for the floats and particles are broadly  
482 consistent, but neither could conclusively categorize the dispersion as local vs non-local. This  
483 consistency is not completely expected, since the Lagrangian frequency spectrum and second order  
484 structure functions indicated that the floats experienced a flow field that was more energetic than  
485 the model, at scales less than roughly a week and 20-30 km. The main issue with the time-  
486 based metrics was that in an effort to have a sufficient number of samples, a relatively large initial  
487 separation had to be selected. Having a large initial separation results in the pairs dispersing to the  
488 uncorrelated scales relatively fast, which does not allow the distinct signatures of the dispersion  
489 regimes to emerge very prominently.

490 The space-based metrics, relative diffusivity and finite size Lyapunov exponents (FSLE), indi-  
491 cated that the dispersion is local for the floats and non-local for the particles, when these metrics  
492 are computed at the sampling time scale of 1 day. For the relative diffusivity, which allows in-  
493 tegration in time, we found that after integrating over timescale of 6 days the relative diffusivity  
494 from the floats had the same characteristics as the relative diffusivity from the particles at scales  
495 larger than 5km. This suggests that the highest frequency motions have little or no impact on dis-  
496 persion. It is not possible to say from float trajectories alone, but it is likely that the high frequency  
497 range is dominated by near inertial waves (NIWs), internal wave continuum and tides. Indepen-  
498 dent observations suggest these high-frequency flows are abundant in the ACC (e.g Ledwell et al.  
499 2011; Waterman et al. 2013; Kilbourne and Garton 2015). Despite having super-inertial frequen-  
500 cies, this wave energy can be aliased into the float positions, which are sampled once a day. We  
501 showed in the appendix A that adding linear waves, which do not add any particle dispersion, to  
502 the non-locally dispersed model particle trajectories can make the space-based metrics to appear  
503 local at length scales that are 20-30 times the displacement amplitude of these waves. Integrating

504 the relative diffusivity in time is found to be a practical way to recover the underlying dispersion  
505 characteristics.

506 Linear waves have relatively little effect on lateral stirring of Lagrangian particles (Holmes-  
507 Cerfon et al. 2011), but they can cause appreciable stirring for a tracer that can diffuse diapycnally  
508 (Young et al. 1982). Previously it was shown that inertial oscillations have a similar minimal effect  
509 with surface drifter pairs, contributing substantial energy to the structure functions at small scales  
510 without impacting lateral dispersion (Beron-Vera and LaCasce 2016). Local stirring at small scales  
511 has been observed in several studies, most comprehensively in the global drifter study of Corrado  
512 et al. (2017). The evidence for this usually comes from space-based metrics. While it is certain  
513 that super-inertial motions affect energy spectra at submesoscales, it remains to be seen to what  
514 extent these motions affect lateral dispersion. At least in the present case, the effect appears to be  
515 small.

516 Our conclusion of non-local dispersion from the floats is also consistent with the behavior of the  
517 tracer released during the DIMES experiment, which showed small irreversible diffusivity during  
518 the initial filamentation phase up to the scales of the mesoscale eddies, and growing irreversible  
519 diffusivity after the tracer filaments start to merge and form a large tracer cloud (Zika et al. 2020).  
520 This is in line with the characteristics of stirring and filamentation in the deep ocean that was  
521 hypothesized by Garrett (1983), and has also been observed in the North Atlantic during NATRE  
522 (Sundermeyer and Price 1998).

523 We cannot entirely discount the possibility that small-scale flows in the interior ocean can lead  
524 to some net dispersion, particularly at the smallest scales ( $<10\text{km}$ ), and the true dispersion might  
525 be in some sense weakly local at these smaller scales. Some recent studies have identified that sub-  
526 mesoscale flows with surface origins can penetrate appreciably below the mixed layer (Yu et al.  
527 2019; Siegelman 2020). Strong submesoscale flows and eddies in interior ocean, without any sur-



528 face association, can also potentially result from interaction between internal waves and balanced  
529 flows (Thomas and Yamada 2019), or result due to breaking waves creating mixed patches that  
530 then coalesce into pancake vortices due to an inverse cascade (Sundermeyer et al. 2005; Polzin  
531 and Ferrari 2004), or be generated by flow interacting with topography and spinning off eddies  
532 (Srinivasan et al. 2019; Vic et al. 2018; Bracco et al. 2016). It is also possible that isobaric floats,  
533 which do not follow water parcels in the vertical, can disperse away from the water parcels that  
534 they were originally tracking (Dewar 1980). However, it seems that the influence of these small-  
535 scale flows, if they are present, does not appear as a first order effect in the metrics and at the  
536 scales considered here, and if these scales are causing any significant stirring then it is not easily  
537 distinguishable from sampling noise and biases. Hence, it is also important to devise new metrics  
538 that will be more sensitive to the stirring at smaller scales.

539 Most current ocean models use diffusive parameterizations (Fox-Kemper et al. 2019), even at  
540 scales where the stirring is not diffusive. Our hope is that the present observations will inspire  
541 new stirring parameterizations (e.g. Kämpf and Cox 2016), along with efforts in improvement of  
542 parameterizations of ocean energetics (Bachman et al. 2017; Zanna 2019), for ocean models that  
543 partially resolve mesoscale eddies.

544 *Acknowledgments.* DB and KS acknowledge support from NSF OCE 1658479 and NSF OCE  
545 1231803, and DB also acknowledges additional support from NSF OCE 1756882. JHL was sup-  
546 ported by by the Rough Ocean project number 302743 under the Norwegian Research Council.  
547 The code for all the analysis and figures is shared at [https://github.com/dhruvbalwada/  
548 mesoscale\\_stirring\\_dimes\\_floats](https://github.com/dhruvbalwada/mesoscale_stirring_dimes_floats), and the processed data can be made available at request  
549 to the corresponding author.

## Impact of Linear Waves on Space-Based and Time-Based Metrics

551

552 Recent studies have shown that the space-based stirring metrics, which average the data into spatial  
553 bins, can sometimes result in misleading conclusions in the presence of linear waves, which do not  
554 cause any net particle dispersion (Beron-Vera and LaCasce 2016), or position errors in trajectories  
555 (Haza et al. 2014). For completeness, and because neither of the previous studies considered all  
556 the metrics together, we demonstrate the biases in conclusions about the stirring regime that can  
557 occur if monochromatic waves are added to the particle trajectories.

558 We modified the position vectors of the particle trajectory pair members ( $\mathbf{X}_i$  and  $\mathbf{X}_j$ ) by adding  
559 oscillations with a single frequency,

$$\begin{aligned}\mathbf{X}_i &\rightarrow \mathbf{X}_i + A(\sin(\omega t + \phi), \cos(\omega t + \phi) - 1) \\ \mathbf{X}_j &\rightarrow \mathbf{X}_j + [A + Bg(r)](\sin(\omega t + \phi), \cos(\omega t + \phi) - 1).\end{aligned}\tag{A1}$$

560 Here  $A$  is the amplitude of the oscillation common to both members, and  $B$  is the difference in the  
561 amplitude for the pair member, with the function  $g(r)$  depending on pair separation ( $r = |\mathbf{X}_i - \mathbf{X}_j|$ ).  
562  $\omega$  is the frequency and  $\phi$  is the starting phase of the waves.  $g(r)$  models the change in amplitude  
563 as the particles move away from each other.  $g(r)$  is modeled as a power law with slope  $n$  below a  
564 length scale  $r_L$  and a constant at larger scales,

$$\begin{aligned}g(r) &= (r/r_L)^n \quad \text{for } r < r_L, \\ &= 1 \quad \text{for } r \geq r_L.\end{aligned}\tag{A2}$$

565 Beron-Vera and LaCasce (2016) employed a similar function in time rather than space, to mimic  
566 inertial oscillations in the Gulf of Mexico.  $A$  and  $B$  are prescribed as random numbers from a  
567 uniform distribution that can vary between  $0 - 2A_{max}$  and  $0 - 2B_{max}$ .  $\phi$  was chosen as a random  
568 number on the interval  $(0, 2\pi)$ .  $\omega$  was set to the local inertial frequency. We experimented with  
569 different choices of the parameters  $(A_{max}, B_{max}, n, r_L)$ , and here we show results for four cases with

570 physically reasonable values;  $A_{max} = 1.5\text{km}$ ,  $r_L = 50\text{km}$ ,  $B_{max} = 2\text{km}$  and  $3.5\text{km}$ , and  $n = 0.3$  and  
571  $0.5$ . These values result in waves that are reasonably close in magnitude to the NIWs measured  
572 in the same region and during the same time as the floats (Kilbourne and Girton 2015). Since the  
573 waves are monochromatic and the inertial frequency ( $\sim 1/(14\text{hours})$ ) is greater than the sampling  
574 frequency ( $\sim 1/(24\text{hours})$ ), the frequency spectrum shows a peak in a narrow band at a lower  
575 frequency where most of the wave signal has been aliased (Figure A1 a). We do not expect such  
576 a pronounced peak in the observations because the waves in the ocean are spread over a wider  
577 frequency range.

578 The space-based stirring metrics estimated using the modified trajectories are qualitatively dif-  
579 ferent from those estimated using the original trajectories (Figure A1 b,d,f). The addition of waves  
580 impacts the metrics significantly, with the range of influence depending on the strength and spatial  
581 correlation of waves. For example the FSLE for  $n=0.5$  and  $B=3.5\text{km}$  (dashed purple line in Fig  
582 A1 f), indicates local dispersion up to scales that are  $\sim 20 - 30$  times larger than the relative am-  
583 plitude of the waves. Thus, high frequency motions due to linear waves preferentially impact the  
584 space-based metrics.

585 The time-based metrics are less affected: the relative dispersion (Figure A1 c), the separation  
586 PDFs and kurtosis (not shown). This is because the added oscillations cancel out when integrated  
587 over time, with the integration time depending on the noise magnitude; Figure A1 c shows that it  
588 takes approximately 5-8 days for the wave contributions to integrate out of the relative dispersion  
589 with  $r_0 = 11\text{km}$ . This initial influence on relative dispersion influences the relative diffusivity -  
590  $\kappa(r)$  (Figure A1 d) when  $\Delta t$  is small. However, waves can be filtered by increasing the  $\Delta t$  used  
591 to estimate the time derivative (Figure A1 e), which allows recovering the sub-inertial signal. We  
592 used the same filtering method in Section 5.

593 The objective here is not to develop a realistic model for the wave effects on the trajectories,  
594 but to simply show that wave motions that do not disperse particle pairs can easily impact some  
595 metrics commonly used to infer the characteristics of pair dispersion. Further, this is meant to  
596 be an Occam's razor approach - if all the small scale motions absent in the model were represented  
597 using only waves that do not disperse particles, could they make the metrics from the model look  
598 similar to the observations within realistic ranges of wave parameters?

## 599 APPENDIX B

### 600 Separation PDFs from Floats and Particles

601 The pair separation PDFs provide direct insight into how the turbulent flow stirs and disperses  
602 floats and particles. For easier visualization we show the cumulative distribution function (CDF),  
603 which is monotonic and varies between 0 and 1.

604 Qualitatively the evolution of the CDFs from the floats and particles is very similar (Figure B1).  
605 Only a small distinction is seen in the initial behavior, when the float CDFs are wider than the  
606 particle CDFs, which is simply a result of the float pairs having a spread over the initial separation  
607 bin. During the first 5-10 days the pair separations spread to both larger and smaller scales than  $r_0$ ,  
608 and after this the pair separations increase on average as the trajectory clusters get more dispersed.  
609 Also during the initial phase the mean pair separation ( $r^*$ ) coincides with the separation where the  
610 CDF is around 0.8~0.9, indicating that the long tails of the PDF are responsible for controlling  
611 the mean pair separation or dispersion. As time progresses  $r^*$  starts to coincide more with smaller  
612 values of the CDF ( $\approx 0.5 \sim 0.6$ ), as is expected for diffusive pair separation. Also, at most times  
613 during the evolution the pairs occupy 1-2 decades of spatial scales, suggesting that the pairs sample  
614 many different turbulent regimes, and the PDFs might only evolve like the theoretical solutions  
615 for short periods of time.

616 We compare the PDFs of the float and particle pairs with the different theoretical solutions using  
617 the two sample Kolmogorov-Smirnov (KS) test, which is used to test the null hypothesis that the  
618 data from two sets of samples comes from the same continuous distribution (Berger and Zhou  
619 2014). It returns a KS statistic or p-value, where a large p-value ( $> 0.05$ ) suggests that the null  
620 hypothesis can not be rejected, implying that the two sets of samples might have been sampled  
621 from the same distribution. Here our first sample set was the separations measured by the float  
622 or particle pairs, while the second sample set was 10000 randomly generated samples using the  
623 theoretical PDF (equations in Table 1).

624 To generate the random samples from the theoretical PDFs, and compare against the float and  
625 particle PDFs, we need two parameters;  $r_0$  and the growth parameters -  $\beta$  for the Richardson or  $T_L$   
626 for the non-local dispersion. We do not assume a priori that one regime is a better descriptor than  
627 the other, instead we estimate the growth parameters corresponding to both regimes and then use  
628 the KS test to check how well do both the theoretical PDFs with the estimated parameters match  
629 the measured separation PDF.

630 The parameter estimation is done by fitting the different theoretical relative dispersion (equations  
631 in Table 1) to the relative dispersion measured by the floats and particles (discussed in Section 4d).  
632 Similar fittings to estimate parameters were done by Graff et al. (2015); Beron-Vera and LaCasce  
633 (2016), where the fitting was done over the time period it took for the mean separation to increase  
634 to some chosen multiple of the initial separation. Here instead of fitting over a specified period,  
635 we fit over a range of times, and test the sensitivity of the parameters and PDF matching between  
636 theory and measurements to choice of the duration over which the fit is done. We fit both the  
637 theoretical curves during the period between day 0 to day  $t_a$ , where  $t_a$  ranges from 3 to 50 days,  
638 using least squares fitting. The parameters are estimated even if the theoretical curve is a poor fit to  
639 the dispersion, but since these parameters also give a poor fit to the PDF they are ruled out by the

640 KS test. Using these estimated parameters (Figure B2) we calculated the KS statistic to compare  
641 the measured PDFs against theoretical PDFs (Figure B3).

642 The comparison of the float PDFs to the theoretical PDFs suggests that for much of the time  
643 the PDFs measured by the floats could correspond to both the Richardson or the non-local PDF  
644 (Figure B3), as  $t_a$  is varied. This result is particularly relevant when  $r_0 = 10 - 15\text{km}$ . The deep  
645 float set released with initial  $r_0 = 30 - 35\text{km}$  is a notable exception; for  $t_a > 20$  days a match  
646 to non-local regime is seen for approximately 10 days followed by a Richardson regime from  
647 approximately 10 to 70 days (Figure B3d and l). This suggests non-local stirring up to scales  
648 of 50km and Richardson like stirring at scales larger than 50km, where the length scale estimate  
649 is based on the mean separation curve in Figure B1d. A similar, but relatively less well defined  
650 behavior is also seen for the shallow float set released with the same initial  $r_0$  (Figure B3b and j).

651 A comparison of the particle PDFs to the theoretical PDFs shows different behavior compared to  
652 the float PDFs. The particle PDFs are better determined due to having significantly larger number  
653 of samples ( $> 1000$  pairs), which results in very short periods over which the measured particle  
654 PDFs comply with any of the two theoretical PDFs. All combinations of  $r_0$  and depths considered  
655 here show a range where the corresponding particle PDF matched with the theoretical PDF for  
656 non-local dispersion (Figure B3e-h). The Richardson PDF does not match the particle PDF at  
657 either of the depths for  $r_0 = 11\text{km}$  (Figure B3m and o), while a match over a very short time  
658 period is seen for  $r_0 = 33\text{km}$  (Figure B3n and p). Notably none of the particle sets matched either  
659 of the theoretical PDFs over the first 5-10 days; this might be because the particles experienced  
660 ballistic dispersion during this time (shown next). Overall, these results suggest that the numerical  
661 model shows non-local dispersion as expected.

662 The relative dispersion from the particles for the first 3-4 days also showed a slower growth  
663 rate than exponential (Figure 5 b and e), which is likely the result of dependence on initial con-

664 ditions and ballistic growth. Trajectory pairs need to lose memory of their initial conditions for  
665 the canonical scaling relationships to be expressed (Babiano et al. 1990; Nicolleau and Yu 2004;  
666 Bourgoïn et al. 2006; Foussard et al. 2017). We quantify the rate of loss of memory of the initial  
667 conditions using a memory index,  $M(t|r_0) = \frac{\langle \mathbf{r} \cdot \mathbf{r}_0 \rangle_{r_0}}{r_0 r^2^{1/2}}$ , which is a measure of correlation between  
668 the pair orientation relative to its initial orientation (Foussard et al. 2017). Both floats and particles  
669 lose memory of their initial orientation as time progresses (Figure B4a).  $M(t)$  for the floats is  
670 almost insensitive to the depth but depends strongly on  $r_0$ , while  $M(t)$  for the particles varies more  
671 strongly with depth and is relatively insensitive to  $r_0$ .

672 During the initial phase, when pairs have not lost memory of their initial conditions, the pairs  
673 disperse ballistically ( $\overline{r^2}(t) = r_0^2(1 + C_1 t^2)$ ). Since different choices of depth and  $r_0$  lead to differ-  
674 ent evolution of  $M(t)$ , we define a time scale,  $\tau_m$ , as the time it take for  $M(t)$  to reach a value of 0.6,  
675 and rescale time using this time scale,  $t_m = t/\tau_m$ . The factor of 0.6 was chosen because it caused  
676 all the different rescaled relative dispersion curves ( $\overline{r^2}(t_m|r_0)/r_0^2 - 1$ ) for the particles to collapse  
677 together during this initial phase (Figure B4d), and also caused  $M(t_m)$  to approximately collapse  
678 (Figure B4b). The particles show a perfect ballistic growth up to approximately  $\sim 0.5t_m$ , after  
679 which the different curves diverge. The range of this ballistic growth is observed approximately  
680 to length scales of  $r^* \approx 2 - 3r_0$ , which are within the numerical model's viscous range. Foussard  
681 et al. (2017) also observed a similar ballistic range in a family of two dimensional numerical mod-  
682 els, and noted that the departure from the ballistic regime seemed to occur around the time that the  
683 mean separation became comparable to the smallest length scales corresponding to the start of the  
684 inertial ranges. The re-scaled relative dispersion curves from the floats did not show such a clear  
685 range of quadratic growth, and were relatively noisy (Figure B4c), which is probably a result of  
686 high-frequency variability resulting in a very rapid loss of memory of initial conditions that is not  
687 properly quantified by  $M(t)$ .

**Relative diffusivity and waves**

Here we show that waves, which can be a dominant part of energy spectrum or the second order structure function at the submesoscales, may not impact the relative diffusivity. As  $\kappa$  is related to the relative velocity auto-correlation, it can be expressed in terms of the wavenumber-frequency energy spectrum (Bennett 1984; Babiano et al. 1990), as

$$\kappa(r,t) = 2 \int_0^\infty \int_0^\infty \left[ E_{ll}(k, \omega) (1 - J_0(kr)) \int_0^t R(k, \omega, \tau) d\tau \right] d\omega dk. \quad (C1)$$

This equation is similar to equation 2 for the longitudinal second order structure function, except that it is weighted by the integral of the normalized wavenumber-frequency Lagrangian energy spectrum  $R(k, \omega, \tau)$ .  $R(k, \omega, \tau)$  is the Lagrangian autocorrelation for flows of wavenumber  $k$  and frequency  $\omega$ , defined as  $R(k, \omega, \tau) = U_{ll}(k, \omega, \tau) / U_{ll}(k, \omega, 0)$ , where

$$U_{ll}(k, \omega, \tau) = \frac{1}{(2\pi)^3} \int \int \int \langle u_l(\mathbf{x} + \mathbf{r}, t + T, t) u_l(\mathbf{x}, t, t - \tau) \rangle \exp(i\mathbf{k} \cdot \mathbf{r} + \omega T) d^2\mathbf{r} dT, \quad (C2)$$

and  $U_{ll}(k, \omega, 0) = (2\pi k)^{-1} E_{ll}(k, \omega)$ .  $u_l(\mathbf{x}, t, t - \tau)$  is the longitudinal velocity at time  $(t - \tau)$  of a trajectory  $\mathbf{r}$  that passes through  $\mathbf{x}$  at time  $t$ , while  $u_l(\mathbf{x} + \mathbf{r}, t + T, t)$  is the longitudinal velocity at time  $t + T$  at a location  $\mathbf{x} + \mathbf{r}$ . The purpose of having two time lags: an Eulerian time ( $T$ ) and a Lagrangian time ( $\tau$ ), in contrast to only a Lagrangian time as in Bennett (1984), is to be able to do a spectral decomposition in frequency. The dependence on  $\mathbf{x}$  and  $t$  on is dropped assuming homogeneity in space and stationarity in time of the underlying Eulerian flow field.

At small times the  $R(k, \omega, \tau)$  is 1, and  $\kappa(r,t) \approx t S_{2ll}(r)$ ; implying that the relative diffusivity and second order structure function follow the same scaling (Babiano et al. 1990). If time is longer than the integral time scales ( $t \gg T_I(\kappa, \omega)$ ) for all wavenumbers and frequencies but smaller than



707 the uncorrelated limit, then the relative diffusivity follows,

$$\kappa(r) = 2 \int_0^\infty \int_0^\infty [E_{II}(k, \omega) T_I(k, \omega) (1 - J_0(kr))] d\omega dk. \quad (\text{C3})$$

708 Here  $T_I(k, \omega) = \int_0^\infty R(k, \omega, \tau) d\tau$  acts as a filter in equation C3, and modulates the extent to which  
709 the  $E_{II}(k, \omega)$  at each wavenumber and frequency impacts the stirring. The integral time scale that is  
710 usually estimated from the single-particle velocity autocorrelation (LaCasce 2008; Balwada et al.  
711 2016b) is equivalent to the integral of  $T_I(k, \omega)$  over all wavenumber and frequency. The estimate  
712 of relative diffusivity in equation 7 is the estimate that we are interested in, since we care about  
713 the integrated impacts of stirring.

714 Since linear waves do not contribute significantly to stirring (Holmes-Cerfon et al. 2011; Bühler  
715 et al. 2013), the wavenumbers and frequencies composed primarily of waves will have  $T_I \approx 0$   
716 and the kinetic energy of these scales will not contribute to the relative diffusivity estimate in  
717 equation 7. Balwada et al. (2018) showed that a conceptually similar result is also true for the  
718 time-mean vertical tracer flux, where the wavenumber-frequency energy spectrum of the vertical  
719 velocity has a dominant peak at the super-inertial frequencies, as a result of linear waves, but  
720 the corresponding cross-spectrum of the vertical tracer flux has no contribution from these scales.  
721 Scaling based estimates of relative diffusivity (discussed towards the end of section 4a), which  
722 stem from 2D turbulence theory, assume the flow is not composed of any linear waves, and thus  
723 all of the kinetic energy spectrum contributes to the relative diffusivity.

## 724 **References**

725 Abernathey, R., and D. Ferreira, 2015: Southern ocean isopycnal mixing and ventilation changes  
726 driven by winds. *Geophysical Research Letters*, **42** (23), 10–357.

- 727 Artale, V., G. Boffetta, A. Celani, M. Cencini, and A. Vulpiani, 1997: Dispersion of passive tracers  
728 in closed basins: Beyond the diffusion coefficient. *Physics of Fluids*, **9 (11)**, 3162–3171.
- 729 Babiano, A., C. Basdevant, P. Le Roy, and R. Sadourny, 1990: Relative dispersion in two-  
730 dimensional turbulence. *Journal of Fluid Mechanics*, **214**, 535–557.
- 731 Babiano, A., C. Basdevant, and R. Sadourny, 1985: Structure functions and dispersion laws in  
732 two-dimensional turbulence. *Journal of the atmospheric sciences*, **42 (9)**, 941–949.
- 733 Bachman, S. D., B. Fox-Kemper, and B. Pearson, 2017: A scale-aware subgrid model for quasi-  
734 geostrophic turbulence. *Journal of Geophysical Research: Oceans*, **122 (2)**, 1529–1554.
- 735 Balwada, D., J. H. LaCasce, and K. G. Speer, 2016a: Scale dependent distribution of kinetic  
736 energy from surface drifters in the gulf of mexico. *Geophysical Research Letters*, n/a–n/a, doi:  
737 10.1002/2016GL069405, URL <http://dx.doi.org/10.1002/2016GL069405>, 2016GL069405.
- 738 Balwada, D., K. S. Smith, and R. Abernathy, 2018: Submesoscale vertical velocities enhance  
739 tracer subduction in an idealized antarctic circumpolar current. *Geophysical Research Letters*,  
740 **45 (18)**, 9790–9802.
- 741 Balwada, D., K. G. Speer, J. H. LaCasce, W. B. Owens, J. Marshall, and R. Ferrari, 2016b:  
742 Circulation and stirring in the southeast pacific ocean and the scotia sea sectors of the  
743 antarctic circumpolar current. *Journal of Physical Oceanography*, **46 (7)**, 2005–2027, doi:10.  
744 1175/JPO-D-15-0207.1, URL <http://dx.doi.org/10.1175/JPO-D-15-0207.1>, [http://dx.doi.org/](http://dx.doi.org/10.1175/JPO-D-15-0207.1)  
745 [10.1175/JPO-D-15-0207.1](http://dx.doi.org/10.1175/JPO-D-15-0207.1).
- 746 Bennett, A., 1984: Relative dispersion: Local and nonlocal dynamics. *Journal of the atmospheric*  
747 *sciences*, **41 (11)**, 1881–1886.
- 748 Bennett, A., 2006: *Lagrangian fluid dynamics*. Cambridge University Press.

- 749 Berger, V. W., and Y. Zhou, 2014: Kolmogorov–smirnov test: Overview. *Wiley statsref: Statistics*  
750 *reference online*.
- 751 Beron-Vera, F. J., and J. H. LaCasce, 2016: Statistics of simulated and observed pair separa-  
752 tions in the gulf of mexico. *Journal of Physical Oceanography*, **46** (7), 2183–2199, doi:10.  
753 1175/JPO-D-15-0127.1, URL <http://dx.doi.org/10.1175/JPO-D-15-0127.1>, [http://dx.doi.org/](http://dx.doi.org/10.1175/JPO-D-15-0127.1)  
754 [10.1175/JPO-D-15-0127.1](http://dx.doi.org/10.1175/JPO-D-15-0127.1).
- 755 Berrisford, P., D. Dee, K. Fielding, M. Fuentes, P. Kallberg, S. Kobayashi, and S. Uppala, 2009:  
756 The era-interim archive. *ERA report series*, (1), 1–16.
- 757 Boland, E. J. D., E. Shuckburgh, P. H. Haynes, J. R. Ledwell, M.-J. Messias, and A. J. Watson,  
758 2015: Estimating a submesoscale diffusivity using a roughness measure applied to a tracer  
759 release experiment in the southern ocean. *Journal of Physical Oceanography*, **45** (6), 1610–  
760 1631, doi:10.1175/JPO-D-14-0047.1, URL <http://dx.doi.org/10.1175/JPO-D-14-0047.1>, [http://](http://dx.doi.org/10.1175/JPO-D-14-0047.1)  
761 [dx.doi.org/10.1175/JPO-D-14-0047.1](http://dx.doi.org/10.1175/JPO-D-14-0047.1).
- 762 Bourgoin, M., N. T. Ouellette, H. Xu, J. Berg, and E. Bodenschatz, 2006: The role of pair disper-  
763 sion in turbulent flow. *Science*, **311** (5762), 835–838.
- 764 Bracco, A., J. Choi, K. Joshi, H. Luo, and J. C. McWilliams, 2016: Submesoscale currents in the  
765 northern gulf of mexico: Deep phenomena and dispersion over the continental slope. *Ocean*  
766 *Modelling*, **101**, 43–58.
- 767 Bühler, O., N. Grisouard, and M. Holmes-Cerfon, 2013: Strong particle dispersion by weakly  
768 dissipative random internal waves. *Journal of Fluid Mechanics*, **719**.

769 Chelton, D. B., R. A. DeSzoeki, M. G. Schlax, K. El Naggar, and N. Siwertz, 1998: Geographical  
770 variability of the first baroclinic rossby radius of deformation. *Journal of Physical Oceanogra-*  
771 *phy*, **28** (3), 433–460.

772 Corrado, R., G. Lacorata, L. Palatella, R. Santoleri, and E. Zambianchi, 2017: General character-  
773 istics of relative dispersion in the ocean. *Scientific Reports*, **7**, 46 291, doi:10.1038/srep46291,  
774 URL <http://www.ncbi.nlm.nih.gov/pmc/articles/PMC5387742/>.

775 Cushman-Roisin, B., 2008: Beyond eddy diffusivity: an alternative model for turbulent dispersion.  
776 *Environmental fluid mechanics*, **8** (5-6), 543–549.

777 Dewar, W. K., 1980: The effect of internal waves on neutrally buoyant floats and other near-  
778 lagrangian tracers. Ph.D. thesis, Massachusetts Institute of Technology.

779 Essink, S., V. Hormann, L. R. Centurioni, and A. Mahadevan, 2019: Can we detect submesoscale  
780 motions in drifter pair dispersion? *Journal of Physical Oceanography*, **49** (9), 2237–2254.

781 Forget, G., 2010: Mapping ocean observations in a dynamical framework: A 2004–06 ocean atlas.  
782 *Journal of Physical Oceanography*, **40** (6), 1201–1221.

783 Foussard, A., S. Berti, X. Perrot, and G. Lapeyre, 2017: Relative dispersion in generalized two-  
784 dimensional turbulence. *Journal of Fluid Mechanics*, **821**, 358–383.

785 Fox-Kemper, B., R. Lumpkin, and F. Bryan, 2013: Lateral transport in the ocean interior. *Ocean*  
786 *Circulation and Climate: A 21st century perspective*, **103**, 185–209.

787 Fox-Kemper, B., and Coauthors, 2019: Challenges and prospects in ocean circulation models.  
788 *Frontiers in Marine Science*, **6**, 65.

789 Garrett, C., 1983: On the initial streakness of a dispersing tracer in two-and three-dimensional  
790 turbulence. *Dynamics of Atmospheres and Oceans*, **7** (4), 265–277.

- 791 Garrett, C., 2006: Turbulent dispersion in the ocean. *Progress in Oceanography*, **70** (2), 113–125.
- 792 Gnanadesikan, A., M.-A. Pradal, and R. Abernathey, 2015: Isopycnal mixing by mesoscale ed-  
793 dies significantly impacts oceanic anthropogenic carbon uptake. *Geophysical Research Let-*  
794 *ters*, **42** (11), 4249–4255, doi:10.1002/2015GL064100, URL file:///Users/dhruvb/Downloads/  
795 ams\_phoc36\_2232.bib, 2015GL064100.
- 796 Graff, L., S. Guttu, and J. LaCasce, 2015: Relative dispersion in the atmosphere from reanalysis  
797 winds. *Journal of the Atmospheric Sciences*, **72** (7), 2769–2785.
- 798 Haza, A. C., T. M. Özgökmen, A. Griffa, A. C. Poje, and M.-P. Lelong, 2014: How does drifter  
799 position uncertainty affect ocean dispersion estimates? *Journal of Atmospheric and Oceanic*  
800 *Technology*, **31** (12), 2809–2828.
- 801 Holmes-Cerfon, M., O. Bühler, and R. Ferrari, 2011: Particle dispersion by random waves in the  
802 rotating boussinesq system. *Journal of fluid mechanics*, **670**, 150–175.
- 803 Jones, C., and R. P. Abernathey, 2019: Isopycnal mixing controls deep ocean ventilation. *Geo-*  
804 *physical Research Letters*, **46** (22), 13 144–13 151.
- 805 Kämpf, J., and D. Cox, 2016: Towards improved numerical schemes of turbulent lateral dispersion.  
806 *Ocean Modelling*, **106**, 1–11.
- 807 Kilbourne, B. F., and J. B. Girton, 2015: Quantifying high-frequency wind energy flux into near-  
808 inertial motions in the southeast pacific. *Journal of Physical Oceanography*, **45** (2), 369–386.
- 809 Koszalka, I., J. LaCasce, M. Andersson, K. Orvik, and C. Mauritzen, 2011: Surface circulation  
810 in the nordic seas from clustered drifters. *Deep Sea Research Part I: Oceanographic Research*  
811 *Papers*, **58** (4), 468–485.

- 812 Koszalka, I., J. LaCasce, and K. Orvik, 2009: Relative dispersion in the nordic seas. *Journal of*  
813 *Marine Research*, **67 (4)**, 411–433.
- 814 LaCasce, J., 2008: Statistics from lagrangian observations. *Progress in Oceanography*, **77 (1)**,  
815 1–29.
- 816 LaCasce, J., 2010: Relative displacement probability distribution functions from balloons and  
817 drifters. *Journal of Marine Research*, **68 (3-4)**, 433–457.
- 818 LaCasce, J., 2016: Estimating eulerian energy spectra from drifters. *Fluids*, **1 (4)**, 33.
- 819 LaCasce, J., and A. Bower, 2000: Relative dispersion in the subsurface north atlantic. *Journal of*  
820 *Marine Research*, **58 (6)**, 863–894.
- 821 LaCasce, J., and C. Ohlmann, 2003: Relative dispersion at the surface of the gulf of mexico.  
822 *Journal of Marine Research*, **61 (3)**, 285–312.
- 823 LaCasce, J. H., R. Ferrari, J. Marshall, R. Tulloch, D. Balwada, and K. Speer, 2014: Float-derived  
824 isopycnal diffusivities in the dimes experiment. *Journal of Physical Oceanography*, **44 (2)**, 764–  
825 780, doi:10.1175/JPO-D-13-0175.1, URL <http://dx.doi.org/10.1175/JPO-D-13-0175.1>, [http://](http://dx.doi.org/10.1175/JPO-D-13-0175.1)  
826 [dx.doi.org/10.1175/JPO-D-13-0175.1](http://dx.doi.org/10.1175/JPO-D-13-0175.1).
- 827 Ledwell, J., E. Montgomery, K. Polzin, L. S. Laurent, R. Schmitt, and J. Toole, 2000: Evidence  
828 for enhanced mixing over rough topography in the abyssal ocean. *Nature*, **403 (6766)**, 179.
- 829 Ledwell, J. R., R. He, Z. Xue, S. F. DiMarco, L. J. Spencer, and P. Chapman, 2016: Dispersion  
830 of a tracer in the deep gulf of mexico. *Journal of Geophysical Research: Oceans*, **121 (2)**,  
831 1110–1132.
- 832 Ledwell, J. R., L. C. St. Laurent, J. B. Girton, and J. M. Toole, 2011: Diapycnal mixing in the  
833 antarctic circumpolar current. *Journal of Physical Oceanography*, **41 (1)**, 241–246.

- 834 Ledwell, J. R., A. J. Watson, and C. S. Law, 1998: Mixing of a tracer in the pycnocline. *Journal*  
835 *of Geophysical Research: Oceans*, **103 (C10)**, 21 499–21 529.
- 836 Lilly, J., 2019: jlab: a data analysis package for matlab, v. 1.6.6. See [http://www. jmlilly.](http://www.jmlilly.net/jmlsoft.html)  
837 [net/jmlsoft. html](http://www.jmlilly.net/jmlsoft.html).
- 838 Lumpkin, R., and S. Elipot, 2010: Surface drifter pair spreading in the north atlantic. *Journal of*  
839 *Geophysical Research: Oceans*, **115 (C12)**.
- 840 Marshall, J., and K. Speer, 2012: Closure of the meridional overturning circulation through south-  
841 ern ocean upwelling. *Nature Geoscience*, **5 (3)**, 171–180.
- 842 Morel, P., and M. Larcveque, 1974: Relative dispersion of constant-level balloons in the 200-mb  
843 general circulation. *Journal of the Atmospheric Sciences*, **31 (8)**, 2189–2196.
- 844 Nicolleau, F., and G. Yu, 2004: Two-particle diffusion and locality assumption. *Physics of Fluids*,  
845 **16 (7)**, 2309–2321.
- 846 Okubo, A., 1971: Oceanic diffusion diagrams. *Deep sea research and oceanographic abstracts*,  
847 Elsevier, Vol. 18, 789–802.
- 848 Ollitrault, M., C. Gabillet, and A. C. De Verdier, 2005: Open ocean regimes of relative dispersion.  
849 *Journal of fluid mechanics*, **533**, 381–407.
- 850 Orsi, A. H., T. Whitworth, and W. D. Nowlin, 1995: On the meridional extent and fronts of  
851 the antarctic circumpolar current. *Deep Sea Research Part I: Oceanographic Research Papers*,  
852 **42 (5)**, 641–673.
- 853 Poje, A. C., and Coauthors, 2014: Submesoscale dispersion in the vicinity of the deepwater hori-  
854 zon spill. *Proceedings of the National Academy of Sciences*, **111 (35)**, 12 693–12 698.

- 855 Polzin, K., and R. Ferrari, 2004: Isopycnal dispersion in nature. *Journal of physical oceanography*,  
856 **34** (1), 247–257.
- 857 Richardson, L. F., 1926: Atmospheric diffusion shown on a distance-neighbour graph. *Proceed-*  
858 *ings of the Royal Society of London. Series A, Containing Papers of a Mathematical and Physi-*  
859 *cal Character*, **110** (756), 709–737.
- 860 Roach, C. J., D. Balwada, and K. Speer, 2016: Horizontal mixing in the southern ocean from argo  
861 float trajectories. *Journal of Geophysical Research: Oceans*, **121** (8), 5570–5586.
- 862 Roach, C. J., D. Balwada, and K. Speer, 2018: Global observations of horizontal mixing from argo  
863 float and surface drifter trajectories. *Journal of Geophysical Research: Oceans*.
- 864 Rossby, T., D. Dorson, and J. Fontaine, 1986: The rafos system. *Journal of Atmospheric and*  
865 *Oceanic Technology*, **3** (4), 672–679.
- 866 Sansón, L. Z., 2015: Surface dispersion in the gulf of california. *Progress in Oceanography*, **137**,  
867 24–37.
- 868 Siegelman, L., 2020: Energetic submesoscale dynamics in the ocean interior. *Journal of Physical*  
869 *Oceanography*, **50** (3), 727–749.
- 870 Sinha, A., D. Balwada, N. Tarshish, and R. Abernathey, 2019: Modulation of lateral transport by  
871 submesoscale flows and inertia-gravity waves. *Journal of Advances in Modeling Earth Systems*,  
872 **11** (4), 1039–1065.
- 873 Srinivasan, K., J. C. McWilliams, M. J. Molemaker, and R. Barkan, 2019: Submesoscale vortical  
874 wakes in the lee of topography. *Journal of Physical Oceanography*, **49** (7), 1949–1971.
- 875 Sundermeyer, M. A., J. R. Ledwell, N. S. Oakey, and B. J. Greenan, 2005: Stirring by small-scale  
876 vortices caused by patchy mixing. *Journal of physical oceanography*, **35** (7), 1245–1262.



877 Sundermeyer, M. A., and J. F. Price, 1998: Lateral mixing and the north atlantic tracer release  
878 experiment: Observations and numerical simulations of lagrangian particles and a passive tracer.  
879 *Journal of Geophysical Research: Oceans*, **103 (C10)**, 21 481–21 497.

880 Swift, D. D., and S. C. Riser, 1994: Rafos floats: Defining and targeting surfaces of neutral  
881 buoyancy. *Journal of atmospheric and Oceanic technology*, **11 (4)**, 1079–1092.

882 Taylor, G. I., 1922: Diffusion by continuous movements. *Proceedings of the london mathematical*  
883 *society*, **2 (1)**, 196–212.

884 Thomas, J., and R. Yamada, 2019: Geophysical turbulence dominated by inertia–gravity waves.  
885 *Journal of Fluid Mechanics*, **875**, 71–100.

886 Thomson, R. E., and W. J. Emery, 2014: *Data analysis methods in physical oceanography*.  
887 Newnes.

888 Tulloch, R., and Coauthors, 2014: Direct estimate of lateral eddy diffusivity upstream of drake  
889 passage. *Journal of Physical Oceanography*, **44 (10)**, 2593–2616.

890 Uchida, T., D. Balwada, R. Abernathey, G. McKinley, S. Smith, and M. Lévy, 2019: The contri-  
891 bution of submesoscale over mesoscale eddy iron transport in the open southern ocean. *Journal*  
892 *of Advances in Modeling Earth Systems*, **11 (12)**, 3934–3958.

893 Uchida, T., D. Balwada, R. P. Abernathey, G. A. McKinley, S. K. Smith, and M. Lévy, 2020:  
894 Vertical eddy iron fluxes support primary production in the open southern ocean. *Nature com-*  
895 *munications*, **11 (1)**, 1–8.

896 van Sebille, E., S. Waterman, A. Barthel, R. Lumpkin, S. R. Keating, C. Fogwill, and C. Turney,  
897 2015: Pairwise surface drifter separation in the western pacific sector of the southern ocean.  
898 *Journal of Geophysical Research: Oceans*, **120 (10)**, 6769–6781.

899 Vic, C., J. Gula, G. Roullet, and F. Pradillon, 2018: Dispersion of deep-sea hydrothermal vent  
900 effluents and larvae by submesoscale and tidal currents. *Deep Sea Research Part I: Oceanographic Research Papers*, **133**, 1–18.

902 Waterman, S., A. C. Naveira Garabato, and K. L. Polzin, 2013: Internal waves and turbulence in  
903 the antarctic circumpolar current. *Journal of Physical Oceanography*, **43** (2), 259–282.

904 Watson, A. J., J. R. Ledwell, M.-J. Messias, B. A. King, N. Mackay, M. P. Meredith, B. Mills, and  
905 A. C. N. Garabato, 2013: Rapid cross-density ocean mixing at mid-depths in the drake passage  
906 measured by tracer release. *Nature*, **501** (7467), 408.

907 Young, W., P. Rhines, and C. Garrett, 1982: Shear-flow dispersion, internal waves and horizontal  
908 mixing in the ocean. *Journal of Physical Oceanography*, **12** (6), 515–527.

909 Yu, X., A. C. Naveira Garabato, A. P. Martin, C. E. Buckingham, L. Brannigan, and Z. Su, 2019:  
910 An annual cycle of submesoscale vertical flow and restratification in the upper ocean. *Journal*  
911 *of Physical Oceanography*, **49** (6), 1439–1461.

912 Zanna, L., 2019: Ocean transport and eddy energy. doi:[https://doi.org/10.6084/m9.figshare.](https://doi.org/10.6084/m9.figshare.10105922.v1)  
913 [10105922.v1](https://doi.org/10.6084/m9.figshare.10105922.v1).

914 Zhurbas, V., and I. S. Oh, 2003: Lateral diffusivity and lagrangian scales in the pacific ocean as  
915 derived from drifter data. *Journal of Geophysical Research: Oceans*, **108** (C5).

916 Zika, J. D., J.-B. Sallée, A. J. S. Meijers, A. C. Naveira-Garabato, A. J. Watson, M.-J. Messias, and  
917 B. A. King, 2020: Tracking the spread of a passive tracer through southern ocean water masses.  
918 *Ocean Science*, **16** (2), 323–336, doi:10.5194/os-16-323-2020, URL [https://www.ocean-sci.net/](https://www.ocean-sci.net/16/323/2020/)  
919 [16/323/2020/](https://www.ocean-sci.net/16/323/2020/).

920 **LIST OF TABLES**

921 **Table 1.** Different dispersion regimes, conditions under which they are applicable, cor-  
 922 responding relative diffusivities (equation 3, 5, section 5, appendix C), PDF  
 923 solutions to the Focker-Plank equation (equation 4, section 4, appendix B), the  
 924 corresponding moments (section 4), and the FSLE scalings (equation 6, section  
 925 6) (Graff et al. 2015; Foussard et al. 2017). The parenthesis note the equations  
 926 and sections where the different metrics are discussed.  $\beta$  is proportional to the  
 927 third root of the energy flux across scales or the energy dissipation rate,  $I_n()$   
 928 is the n-order modified Bessel function,  $M()$  is the Kummer's function,  $T_L$  is  
 929 proportional to the inverse cubic root of the enstrophy dissipation rate or the  
 930 inverse square root of the total enstrophy, and  $C_n$  are constants. . . . . 44

931 **Table 2.** Summary of metrics over scales at which pair velocities are correlated: spatial  
 932 scales smaller than 100km and temporal scales smaller than 50-100days. The  
 933 variability metrics are discussed in section 3, and the stirring metrics in sections  
 934 4 (relative dispersion and kurtosis), 5 (relative diffusivity) and 6 (finite size  
 935 Lyapunov exponents). . . . . 45

936 TABLE 1. Different dispersion regimes, conditions under which they are applicable, corresponding relative  
937 diffusivities (equation 3, 5, section 5, appendix C), PDF solutions to the Focker-Plank equation (equation 4,  
938 section 4, appendix B), the corresponding moments (section 4), and the FSLE scalings (equation 6, section 6)  
939 (Graff et al. 2015; Foussard et al. 2017). The parenthesis note the equations and sections where the different  
940 metrics are discussed.  $\beta$  is proportional to the third root of the energy flux across scales or the energy dissipation  
941 rate,  $I_n()$  is the n-order modified Bessel function,  $M()$  is the Kummer's function,  $T_L$  is proportional to the inverse  
942 cubic root of the enstrophy dissipation rate or the inverse square root of the total enstrophy, and  $C_n$  are constants.

Dispersion Regime	Conditions of validity	Relative Diffusivity ( $\kappa(r,t)$ )	Pair Separation PDF ( $p(r,t r_0)$ )	Relative Dispersion ( $\overline{r^2(t r_0)}$ )	Kurtosis ( $\overline{r^4}/\overline{r^2}^2$ )	FSLE ( $\lambda(r)$ )
Ballistic	Initial time, Memory of initial conditions still present	$tS2_{II}(r)$	-	$r_0^2(1 + C_1 t^2)$	-	-
Non-Local	Intermediate time, $E(k) \sim k^{-3}$ or steeper spectrum	$r^2/T_L$	$\frac{1}{4\pi^{3/2}(t/T_L)^{1/2}r_0^2} \exp\left(-\frac{(\ln r/r_0 + 2t/T)^2}{4t/T_L}\right)$	$r_0^2 \exp\left(\frac{8t}{T_L}\right)$	$e^{8t/T_L}$	$r^0$
Richardson (local)	Intermediate time, $E(k) \sim k^{-5/3}$	$\beta r^{4/3}$	$\frac{3}{4\pi\beta t r_0^{2/3} r^{2/3}} I_2\left(\frac{9r_0^{1/3} r^{1/3}}{2\beta t}\right) \exp\left(-\frac{9(r_0^{2/3} + r^{2/3})}{4\beta t}\right)$	$\frac{5!}{2} \left(\frac{4\beta t}{9}\right)^3 M\left(6, 3, \frac{9r_0^{2/3}}{4\beta t}\right) \exp\left(-\frac{9r_0^{2/3}}{4\beta t}\right)$ , (visually similar to $(r_0^{2/3} + C_2 t)^3$ ) $\sim t^3$ (asymptotic)	5.6 (asymptotic)	$r^{-2/3}$
Diffusive	Long time, pair velocities are uncorrelated	Constant ( $\kappa_2$ )	$\frac{1}{2\pi\kappa_2 t} \exp\left(-\frac{r_0^2 + r^2}{4\kappa_2 t}\right) I_0\left(\frac{r_0 r}{2\kappa_2 t}\right)$	$4\kappa_2 t$ (asymptotic)	2 (asymptotic)	$r^{-2}$

943 TABLE 2. Summary of metrics over scales at which pair velocities are correlated: spatial scales smaller than  
 944 100km and temporal scales smaller than 50-100days. The variability metrics are discussed in section 3, and the  
 945 stirring metrics are discussed in sections 4 (relative dispersion and kurtosis), 5 (relative diffusivity) and 6 (finite  
 946 size Lyapunov exponents).

Variability Metrics	Domain and Averaging	Model Particles	RAFOS Floats	Summary/Comments
Lagrangian Frequency Spectra	Frequency, averaging over all trajectories.	$\omega^{-5\sim-4}$	$\omega^{-4\sim-3}$ ( $\omega < 1/10days$ ); $\omega^{-1\sim-1/2}$ ( $\omega > 1/10days$ )	Enhanced observed variability, likely due to waves aliased to sub-inertial frequencies.
2nd Order Structure Functions	Space-based, averaging over all sample pairs in bin.	$r^2$	$r^{2/3\sim 1}$	Enhanced observed variability, likely due to waves aliased to sub-inertial frequencies.
<b>Stirring Metrics</b>				
Relative Dispersion	Time-based, averaging conditioned on fixed initial pair separation.	Non-local	Consistent with model within errorbars	Limited numbers of float pairs does not allow an unambiguous categorization, but similarity to particles is suggestive of non-local dispersion.
Kurtosis	Time-based, averaging conditioned on fixed initial pair separation.	Non-local	Consistent with model within errorbars	Limited numbers of float pairs does not allow an unambiguous categorization, but similarity to particles is suggestive of non-local dispersion.
Relative Diffusivity	Space-based, averaging over all sample pairs in bin.	$r^2$ ; Non-local	$r^{4/3}$ ( $\Delta t = 1day$ ); $r^{1.5\sim 2}$ ( $\Delta t = 6days$ ) Consistent with model within errorbar at larger $\Delta t$	For floats a steepening of relative diffusivity power law with temporal averaging, to match the particle diffusivity, is highly suggestive of non-local dispersion.
Finite Size Lyapunov Exponents	Space-based, averaging over all sample pairs in bin.	$r^0$ ; Non-local	$r^{-1\sim-2/3}$ ; suggests local	Waves, which do not cause any dispersion, can cause FSLE to appear local even when the dispersion is non-local.

947

## LIST OF FIGURES

948 **Fig. 1.** (a, b) 100 day trajectories of RAFOS floats (a) and a representative set of numerical particles  
949 from the MITgcm simulation (b) at different depths. The green dots indicate the position  
950 of the trajectory on the first day. The climatological Sub-Antarctic Front (SAF) and Polar  
951 Front (PF) are marked by dashed purple lines (Orsi et al. 1995). The gray colors represent  
952 the bathymetry, with the lightest contour color starting at -6000m depth, and increasing by  
953 1000m intervals. (c) The mean longitude of the RAFOS float trajectory pair vs the number of  
954 days since 1 January 2009 at different depths. The first day when the pair formed - when the  
955 two trajectories came within the relative separation threshold - is marked as the green dot.  
956 (d) The mean pressure of the RAFOS float trajectory pair vs the mean difference in pressure  
957 of the two trajectories, averaged over the first 100 days. (e) The number of RAFOS float  
958 pairs as a function of time conditioned on initial separation and in different depth ranges.  
959 (f) The number of RAFOS float pairs as a function of separation distance in different depth  
960 ranges; for statistics where the time evolution of the pair is not tracked. The 'o' markers  
961 indicate the center of the separation bin. . . . . 49

962 **Fig. 2.** Mean Lagrangian frequency rotary spectra from the RAFOS floats between 500-1000m (a)  
963 and 1000-1800m (b). The Mean Lagrangian frequency rotary spectra from the model parti-  
964 cles released at mean depths of 500 and 900m are shown in (a), and at depths of 1100 and  
965 1700m are shown in (b) - the spectra at shallower depth in the model are more energetic.  
966 Power laws of  $\omega^{-3}$  and  $\omega^{-5}$  are also shown in (a) and (b). Second order longitudinal veloc-  
967 ity structure functions for the RAFOS floats and model particles corresponding to the same  
968 depths as (a) and (b) are shown in (c) and (d) respectively. Power laws of  $r^{2/3}$  and  $r^2$   
969 are also shown in (c) and (d). . . . . 50

970 **Fig. 3.** Pair velocity correlations for trajectories at different depths with initial separation of 10-  
971 15km (a) and 30-35km (b). (c) Pair velocity correlations plotted as a function of mean pair  
972 separation ( $r^* = \sqrt{r^2(t)}$ ) showing that correlation curves approximately collapse. Colors  
973 correspond to different depths and different initial separations as indicated in the legends,  
974 while the observational (Obs) floats are marked by solid lines and model (Mod) particles  
975 by dashed lines. Black circles mark the first day for different different the correlation time  
976 series in (c). . . . . 51

977 **Fig. 4.** Isotropy, defined as ratio of mean zonal separation to mean meridional separation for pairs at  
978 different depths - (a) Shallow and (b) Deep - and for different initial separations. (c) Isotropy  
979 ratio plotted as a function of mean pair separation  $r^*$ . . . . . 52

980 **Fig. 5.** Relative dispersion as a function of time for different  $r_0$  and at different depths from the  
981 floats (solid lines) and particles (dashed lines). Top row corresponds to shallow sets and  
982 bottom row to deep sets, and different colors correspond to different sets as indicated in  
983 the legends that are shared between panels. (a,d) show the dispersion on a log-log axis, (b,  
984 e) show the dispersion normalized by the initial dispersion on a semi-log axis for ease of  
985 comparison to non-local dispersion, and (c,f) show the dispersion in a compensated form as  
986 indicated in the axis label for ease of comparison against Richardson dispersion. The gray  
987 lines correspond to the linear (solid) and cubic (dashed) power laws. . . . . 53

988 **Fig. 6.** Kurtosis ( $\overline{r^4}/r_0^2$ ) as a function of time for the floats (solid lines) and the particles (dashed  
989 lines) for different  $r_0$  and depths. Top row corresponds to shallow sets and bottom row to  
990 deep sets, and different colors correspond to different sets as indicated in the legends. The  
991 horizontal lines correspond to the kurtosis for Richardson dispersion (5.6, dashed line) and  
992 simple diffusion (2, solid line). . . . . 54

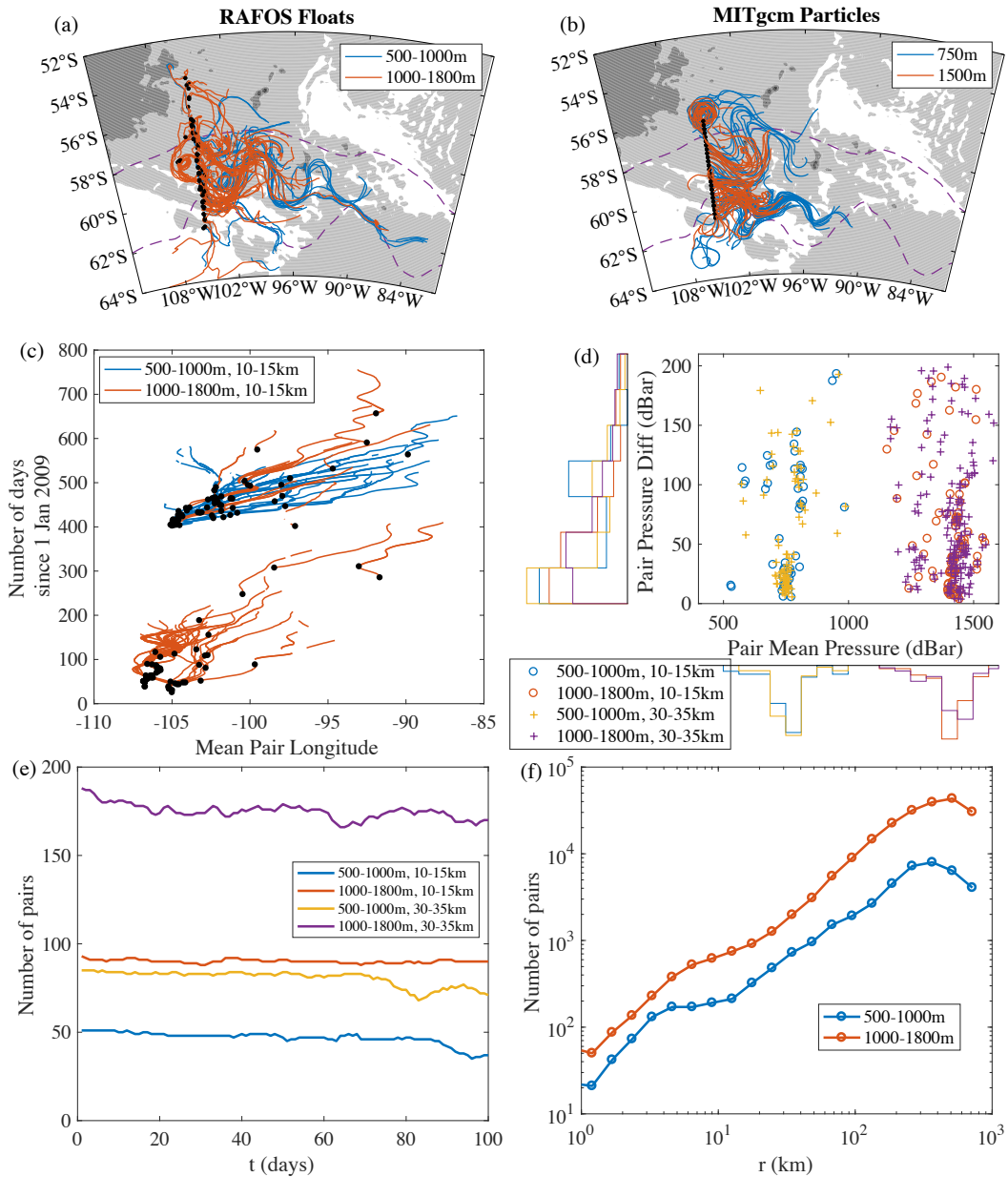
993	<b>Fig. 7.</b>	Relative diffusivity as a function of separation scale. Shallow (a) and deep (b) estimates of $\kappa(r)$ , for the floats and particles with $\Delta t$ of 1 and 6 days. (c) Slope of the relative diffusivity curve between 6-50km as a function of $\Delta t$ . The horizontal gray lines are the values of the slope corresponding to non-local (2, solid) and Richardson (4/3, dashed) dispersion. (d) Relative diffusivity estimated as $\kappa(r^*, r_0)$ for the deep floats and particles, with $\Delta t$ of 6 days. The gray lines correspond to the power laws expected for non-local (solid) and Richardson (dashed) dispersion. The position of these gray lines is the same in the three panels, and can be used to compare the estimates more easily. . . . .	55
1001	<b>Fig. 8.</b>	The zonal and meridional relative diffusivity ( $\kappa(r)$ ) for the shallow (a) and deep (c) floats and particles, estimated with $\Delta t$ of 6 days. The short black line at 500km corresponds to twice the single particle diffusivity from Balwada et al. (2016b). The gray lines correspond to the power laws expected for non-local (solid) and Richardson (dashed) dispersion. The meridional relative diffusivity for the shallow (b) and deep (d) floats as a function of separation and $\Delta t$ is contoured. Values of 100 and 1000 $m^2/s$ are contoured using dashed white lines. . . . .	56
1008	<b>Fig. 9.</b>	Finite scale Lyapunov Exponents as a function of scale for the shallow and deep sets of trajectories from the floats (solid line) and particles (dashed line). The dashed lines correspond to different theoretical expectations; non-local ( $r^0$ ), Richardson ( $r^{-2/3}$ ) and simple diffusion ( $r^{-2}$ ). . . . .	57
1012	<b>Fig. A1.</b>	The impact of adding monochromatic waves with inertial frequency to model trajectories on different metrics: Lagrangian frequency spectrum (a), longitudinal structure function (b), relative dispersion (c), relative diffusivity with $dT = 1$ day (d) and with $dT = 6$ days (e), and finite scale Lyapunov exponent (f). All plots have data from five sets of trajectories: the original trajectories at a depth of 1500m and the same with added waves of different spatial properties, as noted in legend in (a). In (b),(d),(e) and (f) some lines corresponding to standard scalings are also added in gray. . . . .	58
1019	<b>Fig. B1.</b>	Pair separation cumulative distribution functions for the floats (top row - a,b,c,d) and particles (bottom row - e,f,g,h). Each panel corresponds to a different depth and different $r_0$ , as indicated in the panel titles. The contour colorbar ranges from 0 to 1, with increment steps of 0.1. The 0.1, 0.5 and 0.9 contours are marked with dashed black lines, while the mean pair separation is the solid blue line. . . . .	59
1024	<b>Fig. B2.</b>	Theoretical parameters $T_L$ (a) and $\beta$ (b) estimated by fitting measured relative dispersion with theoretical relative dispersion (Table 1). Different depths and initial separations are indicated by colors, while the parameters estimated using floats are marked by solid lines and the parameters estimated using the particles are marked by dashed lines. (a) and (b) share their legends. . . . .	60
1029	<b>Fig. B3.</b>	Kolmogrov-Smirnov test statistic comparing the measured PDFs to the theoretical PDFs, plotted as a function of time and time over which the relative dispersion is fit to estimate the parameters ( $t_a$ ). A value greater than 0.05, marked by black contour line, suggests that the measured and theoretical PDFs are statistically similar. Rows 1 and 3 (a-d and i-l) compare the float PDFs to the non-local and Richardson dispersion, while rows 2 and 4 (e-h and m-p) compare the particle PDFs to the non-local and Richardson dispersion. The dashed blue vertical line corresponds to the time when the mean pair separation ( $r^*$ ) reaches 100km. The depth and initial separation ( $r_0$ ) is indicated in the panel titles. . . . .	61
1037	<b>Fig. B4.</b>	(a) The memory index, quantifying how quickly the dependence on initial condition is lost for all different choices of depth and $r_0$ . The legend for all the figures in shown in (b). (b)	

1039  
1040  
1041  
1042  
1043

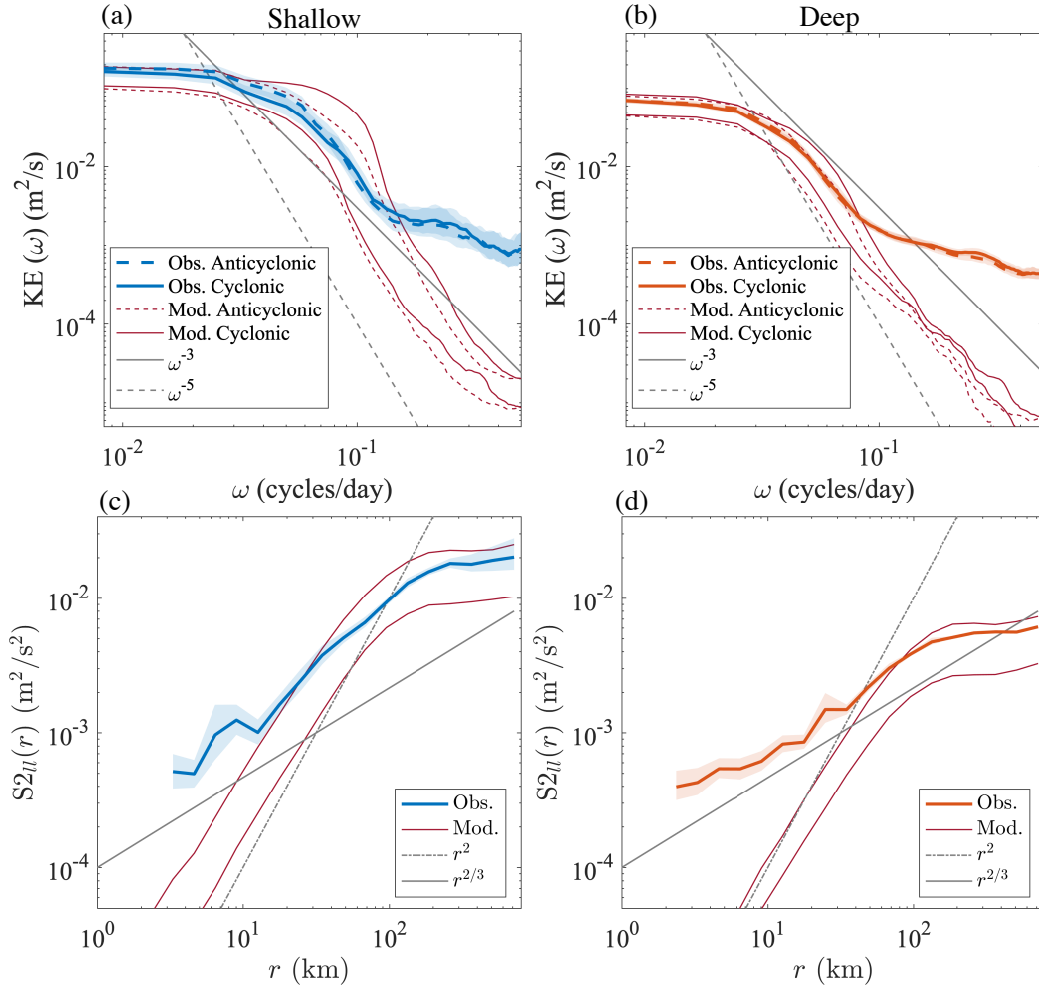
The memory index plotted as a function of rescaled time  $t_m = t/\tau_m$ , where  $\tau_m$  is the time it takes for  $M(t)$  to reach a value of 0.6. Float (c) and particle (d) relative dispersion plotted in compensated form as a function of rescaled time ( $t_m$ ), to identify if a ballistic regime is observed. In (c) and (d) power laws have been plotted for reference as labeled in the legend in panel (d).

62

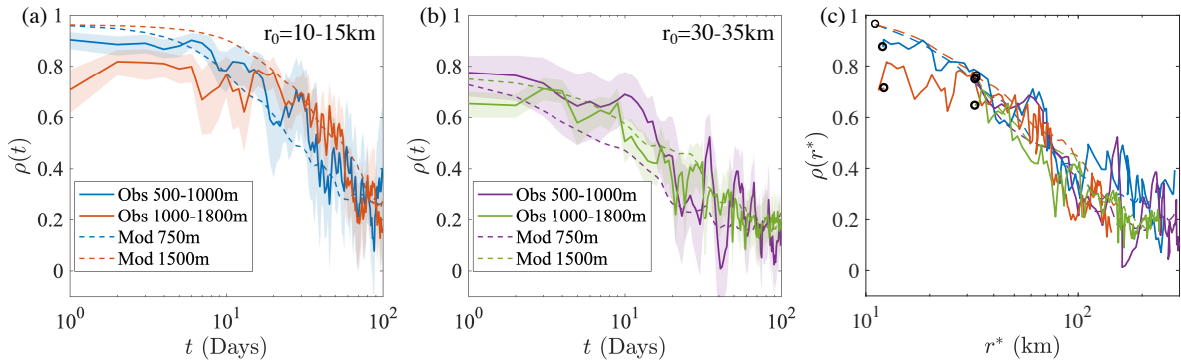




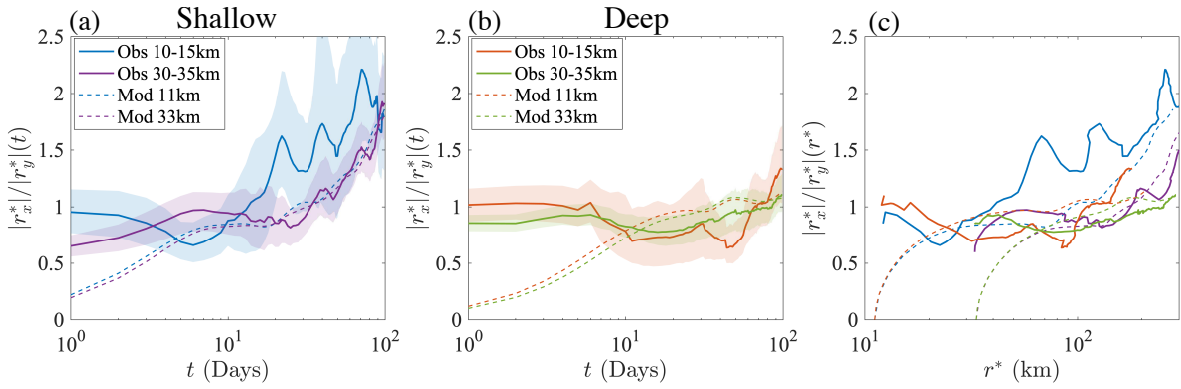
1044 FIG. 1. (a, b) 100 day trajectories of RAFOS floats (a) and a representative set of numerical particles from  
 1045 the MITgcm simulation (b) at different depths. The green dots indicate the position of the trajectory on the first  
 1046 day. The climatological Sub-Antarctic Front (SAF) and Polar Front (PF) are marked by dashed purple lines  
 1047 (Orsi et al. 1995). The gray colors represent the bathymetry, with the lightest contour color starting at -6000m  
 1048 depth, and increasing by 1000m intervals. (c) The mean longitude of the RAFOS float trajectory pair vs the  
 1049 number of days since 1 January 2009 at different depths. The first day when the pair formed - when the two  
 1050 trajectories came within the relative separation threshold - is marked as the green dot. (d) The mean pressure  
 1051 of the RAFOS float trajectory pair vs the mean difference in pressure of the two trajectories, averaged over the  
 1052 first 100 days. (e) The number of RAFOS float pairs as a function of time conditioned on initial separation and  
 1053 in different depth ranges. (f) The number of RAFOS float pairs as a function of separation distance in different



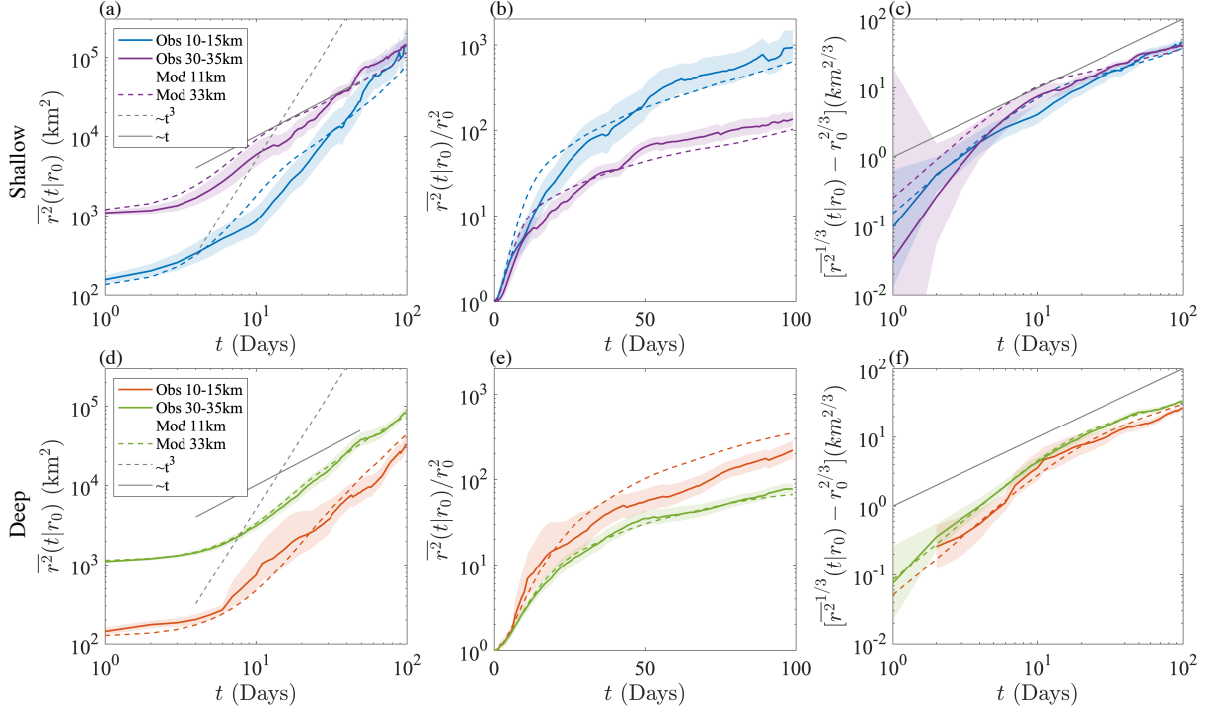
1056 FIG. 2. Mean Lagrangian frequency rotary spectra from the RAFOS floats between 500-1000m (a) and 1000-  
 1057 1800m (b). The Mean Lagrangian frequency rotary spectra from the model particles released at mean depths of  
 1058 500 and 900m are shown in (a), and at depths of 1100 and 1700m are shown in (b) - the spectra at shallower  
 1059 depth in the model are more energetic. Power laws of  $\omega^{-3}$  and  $\omega^{-5}$  are also shown in (a) and (b). Second order  
 1060 longitudinal velocity structure functions for the RAFOS floats and model particles corresponding to the same  
 1061 depths as (a) and (b) are shown in (c) and (d) respectively. Power laws of  $r^{2/3}$  and  $r^2$  are also shown in (c) and  
 1062 (d).



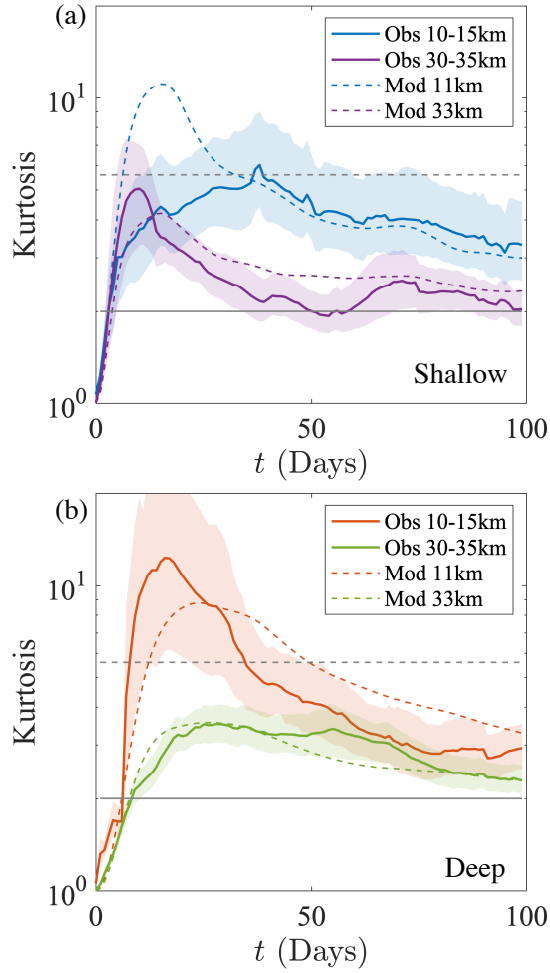
1063 FIG. 3. Pair velocity correlations for trajectories at different depths with initial separation of 10-15km (a)  
 1064 and 30-35km (b). (c) Pair velocity correlations plotted as a function of mean pair separation ( $r^* = \sqrt{r^2(t)}$ )  
 1065 showing that correlation curves approximately collapse. Colors correspond to different depths and different  
 1066 initial separations as indicated in the legends, while the observational (Obs) floats are marked by solid lines and  
 1067 model (Mod) particles by dashed lines. Black circles mark the first day for different different the correlation  
 1068 time series in (c).



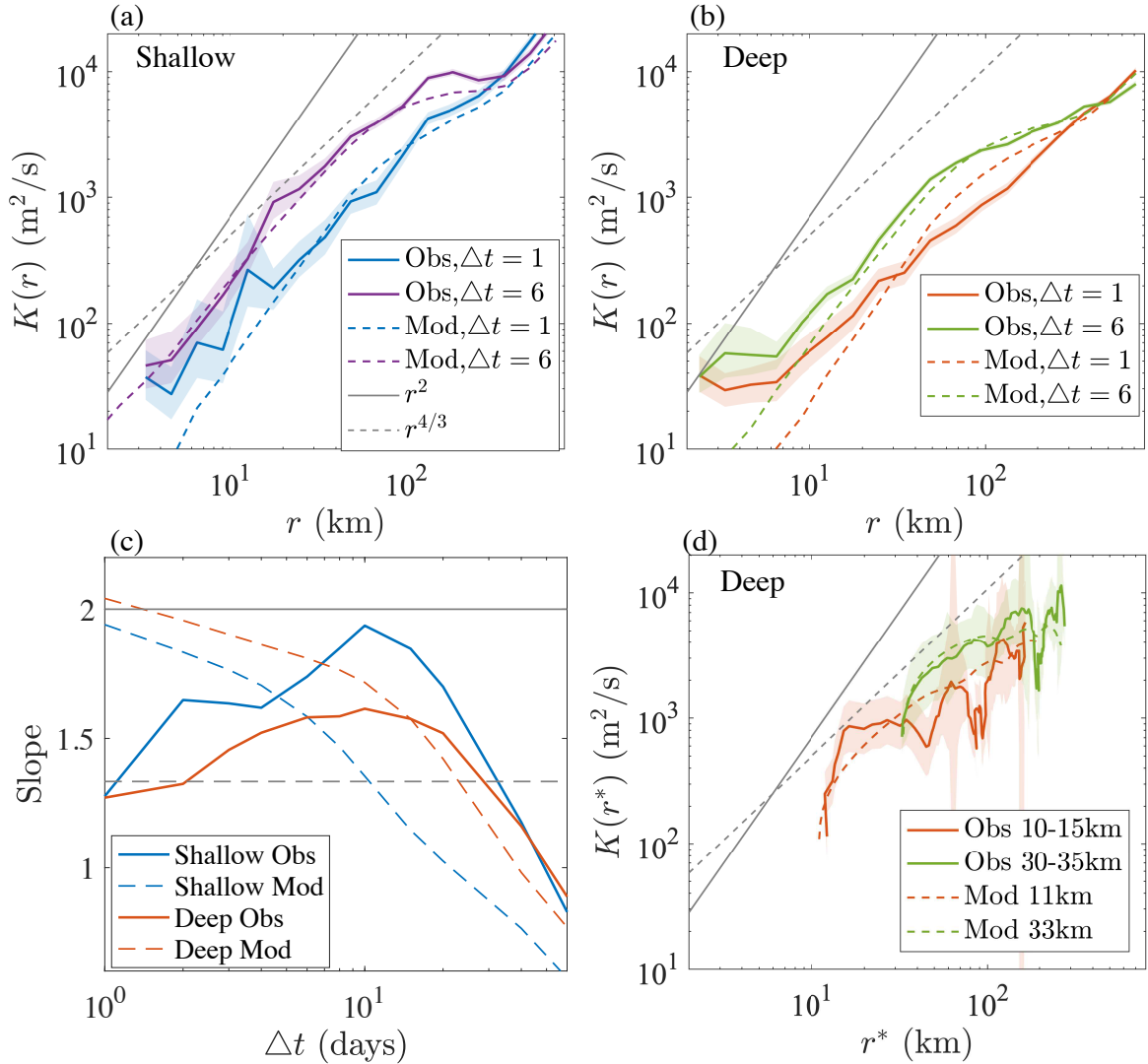
1069 FIG. 4. Isotropy, defined as ratio of mean zonal separation to mean meridional separation for pairs at different  
 1070 depths - (a) Shallow and (b) Deep - and for different initial separations. (c) Isotropy ratio plotted as a function  
 1071 of mean pair separation  $r^*$ .



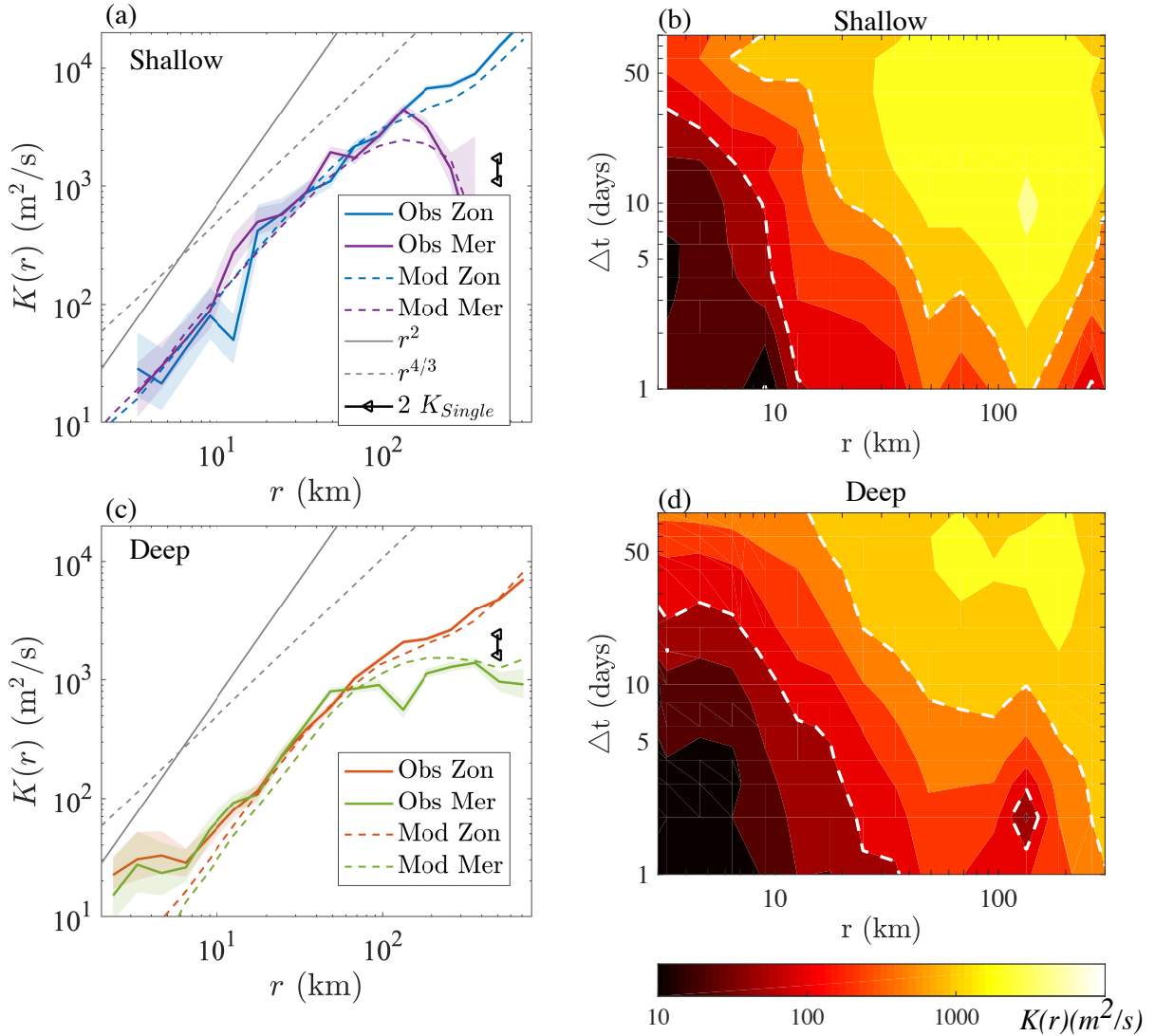
1072 FIG. 5. Relative dispersion as a function of time for different  $r_0$  and at different depths from the floats (solid  
 1073 lines) and particles (dashed lines). Top row corresponds to shallow sets and bottom row to deep sets, and  
 1074 different colors correspond to different sets as indicated in the legends that are shared between panels. (a,d)  
 1075 show the dispersion on a log-log axis, (b, e) show the dispersion normalized by the initial dispersion on a semi-  
 1076 log axis for ease of comparison to non-local dispersion, and (c,f) show the dispersion in a compensated form as  
 1077 indicated in the axis label for ease of comparison against Richardson dispersion. The gray lines correspond to  
 1078 the linear (solid) and cubic (dashed) power laws.



1079 FIG. 6. Kurtosis ( $\overline{r^4}/\overline{r^2}^2$ ) as a function of time for the floats (solid lines) and the particles (dashed lines)  
 1080 for different  $r_0$  and depths. Top row corresponds to shallow sets and bottom row to deep sets, and different  
 1081 colors correspond to different sets as indicated in the legends. The horizontal lines correspond to the kurtosis for  
 1082 Richardson dispersion (5.6, dashed line) and simple diffusion (2, solid line).

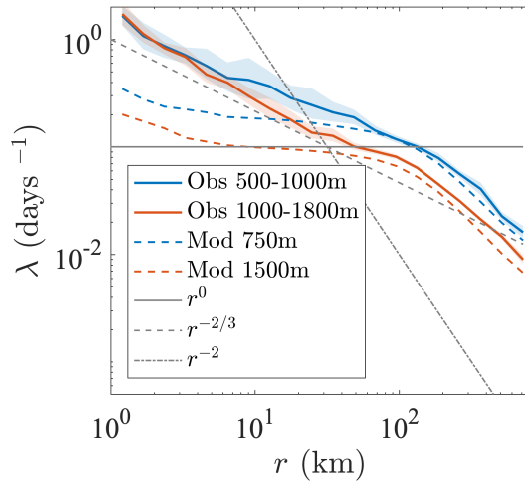


1083 FIG. 7. Relative diffusivity as a function of separation scale. Shallow (a) and deep (b) estimates of  $\kappa(r)$ , for  
 1084 the floats and particles with  $\Delta t$  of 1 and 6 days. (c) Slope of the relative diffusivity curve between 6-50km as  
 1085 a function of  $\Delta t$ . The horizontal gray lines are the values of the slope corresponding to non-local (2, solid)  
 1086 and Richardson (4/3, dashed) dispersion. (d) Relative diffusivity estimated as  $\kappa(r^*, r_0)$  for the deep floats and  
 1087 particles, with  $\Delta t$  of 6 days. The gray lines correspond to the power laws expected for non-local (solid) and  
 1088 Richardson (dashed) dispersion. The position of these gray lines is the same in the three panels, and can be used  
 1089 to compare the estimates more easily.

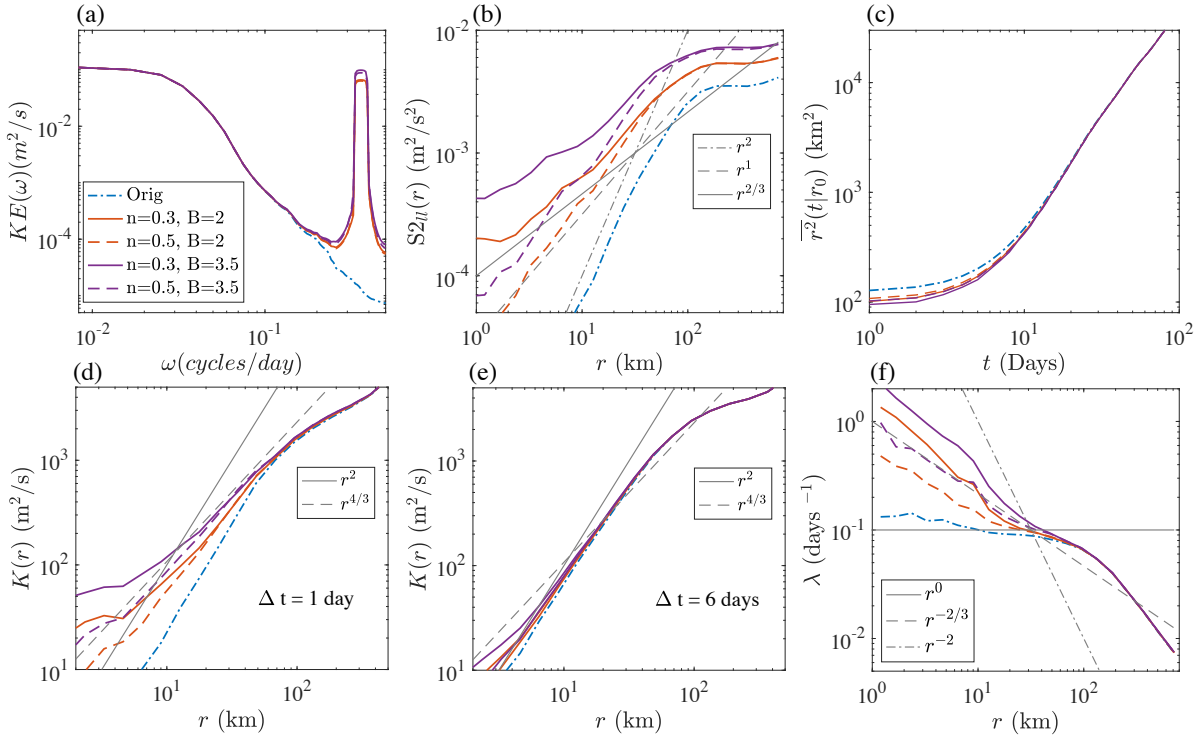


1090 FIG. 8. The zonal and meridional relative diffusivity ( $\kappa(r)$ ) for the shallow (a) and deep (c) floats and particles,  
 1091 estimated with  $\Delta t$  of 6 days. The short black line at 500km corresponds to twice the single particle diffusivity  
 1092 from Balwada et al. (2016b). The gray lines correspond to the power laws expected for non-local (solid) and  
 1093 Richardson (dashed) dispersion. The meridional relative diffusivity for the shallow (b) and deep (d) floats as  
 1094 a function of separation and  $\Delta t$  is contoured. Values of 100 and 1000  $m^2/s$  are contoured using dashed white  
 1095 lines.

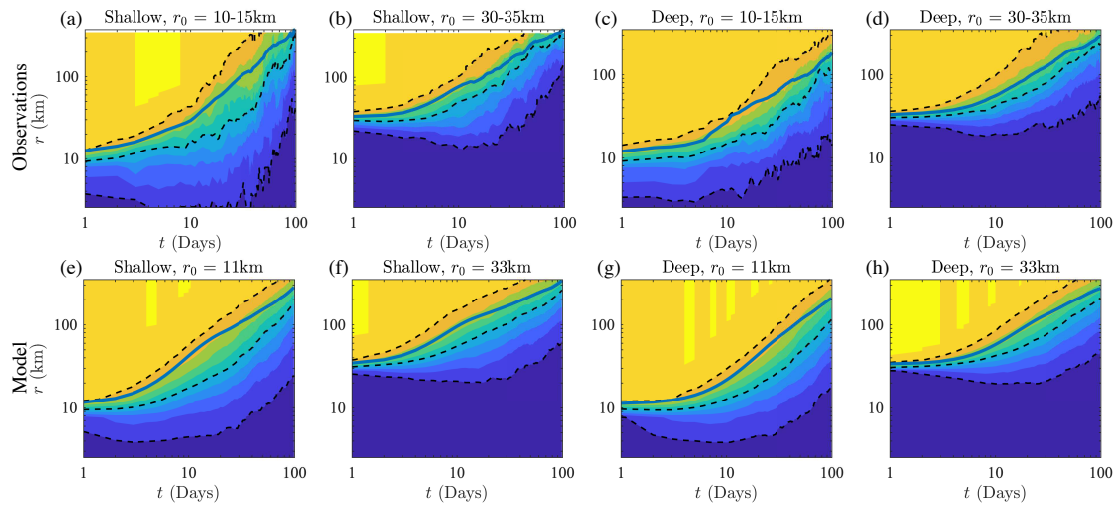




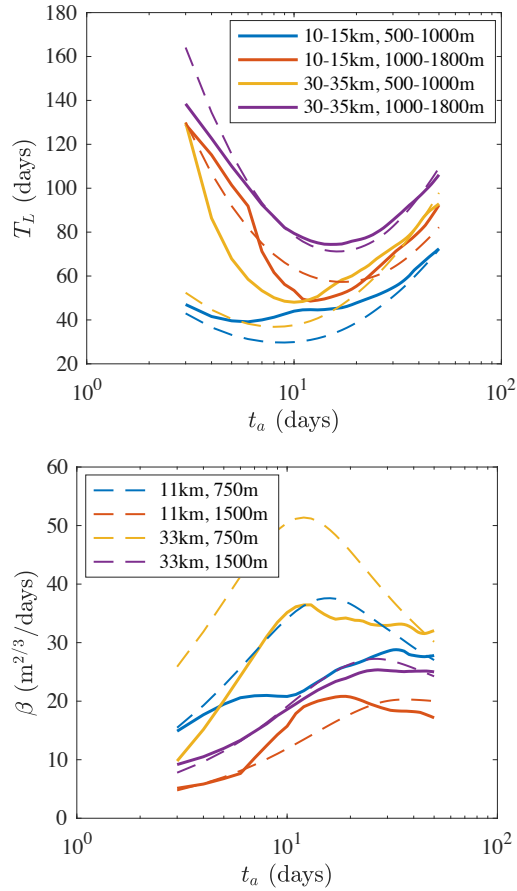
1096 FIG. 9. Finite scale Lyapunov Exponents as a function of scale for the shallow and deep sets of trajectories  
 1097 from the floats (solid line) and particles (dashed line). The dashed lines correspond to different theoretical  
 1098 expectations; non-local ( $r^0$ ), Richardson ( $r^{-2/3}$ ) and simple diffusion ( $r^{-2}$ ).



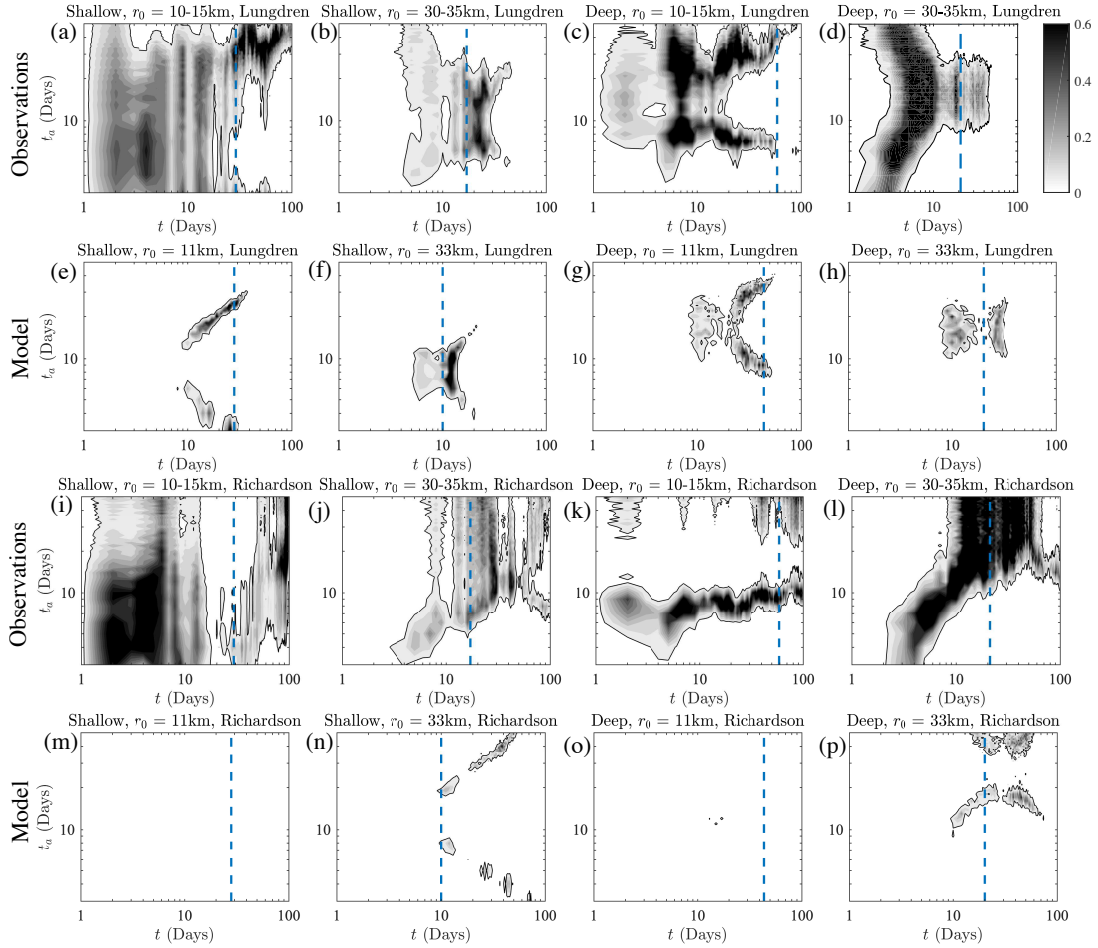
1099 Fig. A1. The impact of adding monochromatic waves with inertial frequency to model trajectories on  
 1100 different metrics: Lagrangian frequency spectrum (a), longitudinal structure function (b), relative dispersion  
 1101 (c), relative diffusivity with  $dT = 1$  day (d) and with  $dT = 6$  days (e), and finite scale Lyapunov exponent (f).  
 1102 All plots have data from five sets of trajectories: the original trajectories at a depth of 1500m and the same with  
 1103 added waves of different spatial properties, as noted in legend in (a). In (b),(d),(e) and (f) some lines  
 1104 corresponding to standard scalings are also added in gray.



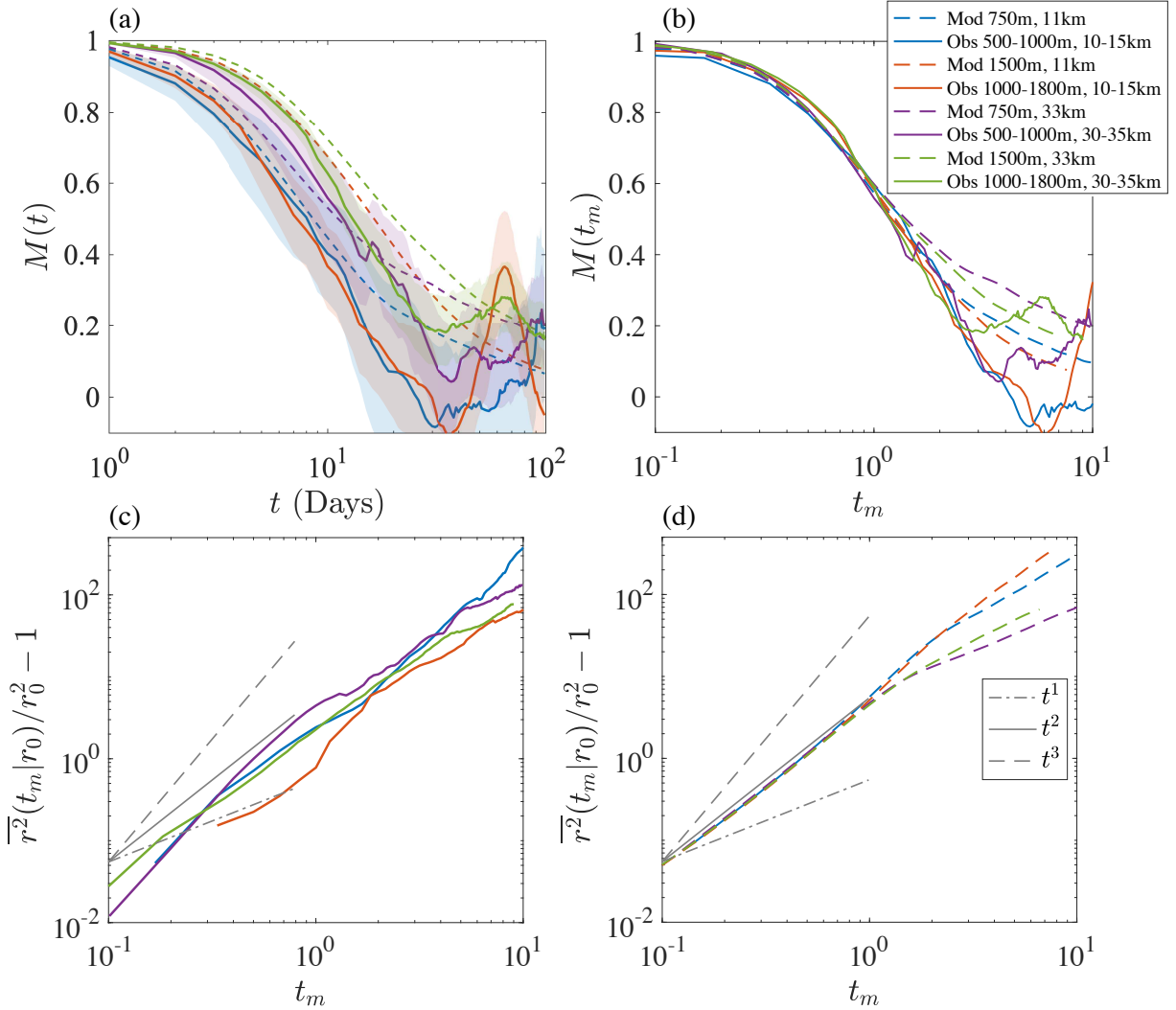
1105 Fig. B1. Pair separation cumulative distribution functions for the floats (top row - a,b,c,d) and particles  
 1106 (bottom row - e,f,g,h). Each panel corresponds to a different depth and different  $r_0$ , as indicated in the panel  
 1107 titles. The contour colorbar ranges from 0 to 1, with increment steps of 0.1. The 0.1, 0.5 and 0.9 contours are  
 1108 marked with dashed black lines, while the mean pair separation is the solid blue line.



1109 Fig. B2. Theoretical parameters  $T_L$  (a) and  $\beta$  (b) estimated by fitting measured relative dispersion with  
 1110 theoretical relative dispersion (Table 1). Different depths and initial separations are indicated by colors, while  
 1111 the parameters estimated using floats are marked by solid lines and the parameters estimated using the particles  
 1112 are marked by dashed lines. (a) and (b) share their legends.



1113 Fig. B3. Kolmogorov-Smirnov test statistic comparing the measured PDFs to the theoretical PDFs, plotted as  
 1114 a function of time and time over which the relative dispersion is fit to estimate the parameters ( $t_a$ ). A value  
 1115 greater than 0.05, marked by black contour line, suggests that the measured and theoretical PDFs are  
 1116 statistically similar. Rows 1 and 3 (a-d and i-l) compare the float PDFs to the non-local and Richardson  
 1117 dispersion, while rows 2 and 4 (e-h and m-p) compare the particle PDFs to the non-local and Richardson  
 1118 dispersion. The dashed blue vertical line corresponds to the time when the mean pair separation ( $r^*$ ) reaches  
 1119 100km. The depth and initial separation ( $r_0$ ) is indicated in the panel titles.



1120 Fig. B4. (a) The memory index, quantifying how quickly the dependence on initial condition is lost for all  
 1121 different choices of depth and  $r_0$ . The legend for all the figures in shown in (b). (b) The memory index plotted  
 1122 as a function of rescaled time  $t_m = t/\tau_m$ , where  $\tau_m$  is the time it takes for  $M(t)$  to reach a value of 0.6. (c)  
 1123 and (d) relative dispersion plotted in compensated form as a function of rescaled time ( $t_m$ ), to identify if  
 1124 a ballistic regime is observed. In (c) and (d) power laws have been plotted for reference as labeled in the legend  
 1125 in panel (d).